

SYNTHESIS OF LONSDALEITE BY FILAMENT-  
ASSISTED CHEMICAL VAPOR DEPOSITION

By

KAREN ELAINE SUHM

Bachelor of Science

Oklahoma State University


Stillwater, Oklahoma

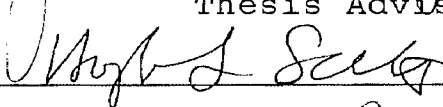
1991

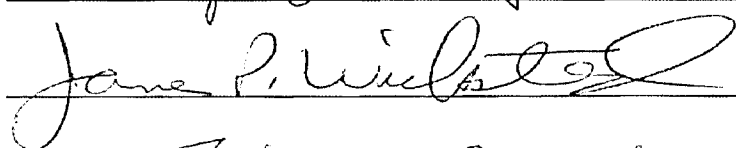
Submitted to the Faculty of the  
Graduate College of the  
Oklahoma State University  
in partial fulfillment of  
the requirements for  
the Degree of  
MASTER OF SCIENCE  
December, 1993


SYNTHESIS OF LONSDALEITE BY FILAMENT-  
ASSISTED CHEMICAL VAPOR DEPOSITION

Thesis Approved:

  
\_\_\_\_\_  
Thesis Advisor

  
\_\_\_\_\_

  
\_\_\_\_\_

  
\_\_\_\_\_  
Dean of the Graduate College

## ACKNOWLEDGEMENTS

I would like to express my sincere gratitude to my thesis advisor, Dr. J. N. Lange, for his guidance, patience, and unfaltering faith in me, even when things seemed weary and desolate. Not once during the bleaker moments of this study did Dr. Lange question my competency, or lack thereof.

I would also like to thank Dr. J. P. Wickstead for his permission to use the Raman spectrometer and for serving on my thesis committee, Dr. J. J. Martin, for the use of his microscope, diamond saw, and almost everything else in his lab, and Mike Lucas and all the guys in the machine shop, without whom this thesis would never have been possible. Thanks also go to Dr. H. L. Scott for serving on my thesis committee.

I must not forget at this point to thank my family and friends for their interest, curiosity, and endless questions about my progress. You people amused, abused, and annoyed me, but certainly spared me from boredom. Special thanks go to my husband, Jerry Little, for assisting me with illustrations, and to my parents, for trying not to sit at the kitchen table when I was working there.

## TABLE OF CONTENTS

Chapter	Page
I. INTRODUCTION.....	1
II. REVIEW OF THE LITERATURE.....	9
Synthesis of Crystalline Carbon by Chemical Vapor Deposition.....	9
Carbide or Carbon Layer Formation.....	10
Nucleation.....	11
Growth.....	14
Failure to Produce Lonsdaleite.....	18
III. SAMPLE PRODUCTION.....	22
Experimental Apparatus.....	22
Procedure.....	24
IV. RAMAN SPECTROSCOPY.....	26
Theory.....	26
Basic Theory.....	27
Polarizability Theory.....	28
Experimental Apparatus.....	30
Procedure.....	33
V. EXPERIMENTAL RESULTS AND ANALYSIS.....	35
Reported Raman Signatures of the Allotropes of Carbon.....	35
Results of Sample Production.....	41
Lonsdaleite.....	43
Diamond.....	45
Other Allotropes of Carbon.....	48
Tungsten Carbide.....	52
VI. DISCUSSION.....	57
VII. SUMMARY AND SUGGESTIONS FOR FUTURE RESEARCH.....	60
REFERENCES.....	62

LIST OF TABLES

Table	Page
I. Summary of Chemical Vapor Deposition Growth Parameters for All Samples.....	36
II. Summary of Reported Raman Peak Positions and Peak Widths for Various Allotropic Forms of Carbon.....	39

## LIST OF FIGURES

Figure	Page
1. Structure of Graphite.....	2
2. Structure of Diamond.....	4
3. Structure of Lonsdaleite.....	5
4. Stacking Sequences of Diamond and Lonsdaleite.....	7
5. Hydrocarbon Cage Compounds Proposed as Nuclei (top) and Associated Twinned Diamond Particles (bottom).....	13
6. Proposed Model of the Growth Mechanism of Diamond: the removal of a surface bonded hydrogen ion by atomic hydrogen (top), followed by the reaction of a surface carbon radical with a hydrocarbon species in the gas phase (bottom).....	19
7. Experimental Filament-Assisted Chemical Vapor Deposition Apparatus Used for Sample Production...	23
8. Experimental Apparatus for Raman Spectroscopy.....	31
9. Graph of Flow Rate Versus Methane Concentration for All Samples, Labeled by Sample Number.....	37
10. Typical Raman Spectrum of Natural Diamond.....	40
11. Typical Raman Spectrum of Graphite.....	42
12. Typical Raman Spectrum of Lonsdaleite Produced in the Present Study.....	44
13. Typical Raman Spectrum of Diamond Produced in the Present Study.....	47
14. Typical Raman Spectrum of Graphite Produced in the Present Study.....	49
15. Typical Raman Spectrum of Microcrystalline Carbon Produced in the Present Study.....	51

Figure	Page
16. Typical Raman Spectrum of the Amorphous Carbon and Microcrystalline Carbon Mixture Produced in the Present Study.....	53
17. Recurring Raman Spectrum of Samples Produced Before CVD Apparatus was Perfected.....	55
18. Typical Raman Spectrum of Tungsten Carbide.....	56
19. Proposed Growth Mechanism for Lonsdaleite: hydrogen ions stabilizing bonds at the lonsdaleite surface (top) are removed by atomic hydrogen, allowing reactions between surface carbon radicals and vapor-phase hydrocarbons (middle), which eventually result in the creation of new lonsdaleite units (bottom).....	59

## NOMENCLATURE

a-C	amorphous carbon
alpha	polarizability
CH <sub>3</sub> <sup>+</sup>	methyl radical
CH <sub>4</sub>	methane
C <sub>2</sub> H <sub>2</sub>	acetylene
C <sub>2</sub> H <sub>4</sub>	ethylene
CVD	chemical vapor deposition
<b>E</b>	applied electric field
<b>E<sub>0</sub></b>	amplitude of applied electric field
FWHM	full width of peak at half maximum height of peak
h	Planck's constant
H <sup>+</sup>	atomic hydrogen
H <sub>2</sub>	molecular hydrogen
M	induced dipole moment
ν	frequency
sccm	standard cubic centimeters per minute



## CHAPTER 1

### INTRODUCTION

The carbon atom has the ground state electron configuration  $1s^2 2s^2 2p^2$  (1) and so has four electrons and four vacancies in its valence band. The two half-filled 2p orbitals will normally bond covalently with other atoms, while the two 2s orbital electrons may bond in a number of ways (2). As a result, there are several allotropic forms of crystalline carbon, including graphite, diamond, lonsdaleite, microcrystalline carbon, and amorphous carbon. Other allotropes include such complicated structures as 6H, 12H, and 20H hexagonal diamond (3,4) and C-60, although they have little bearing on this paper. Each allotrope is unique in structure and its utilization of different types of bonding between atoms.

Graphite, the most common form of carbon, is most frequently found in the hexagonal structure, although it also occurs in rhombohedral form (5). The structure of hexagonal graphite, which is displayed in Figure 1, consists of basal planes of six-membered rings in the AB AB AB... sequence. In the basal plane, the carbon atoms are arranged in a trigonal  $sp^2$  configuration, with three of the valence electrons engaged in  $\sigma$  bonds with neighboring atoms. The fourth

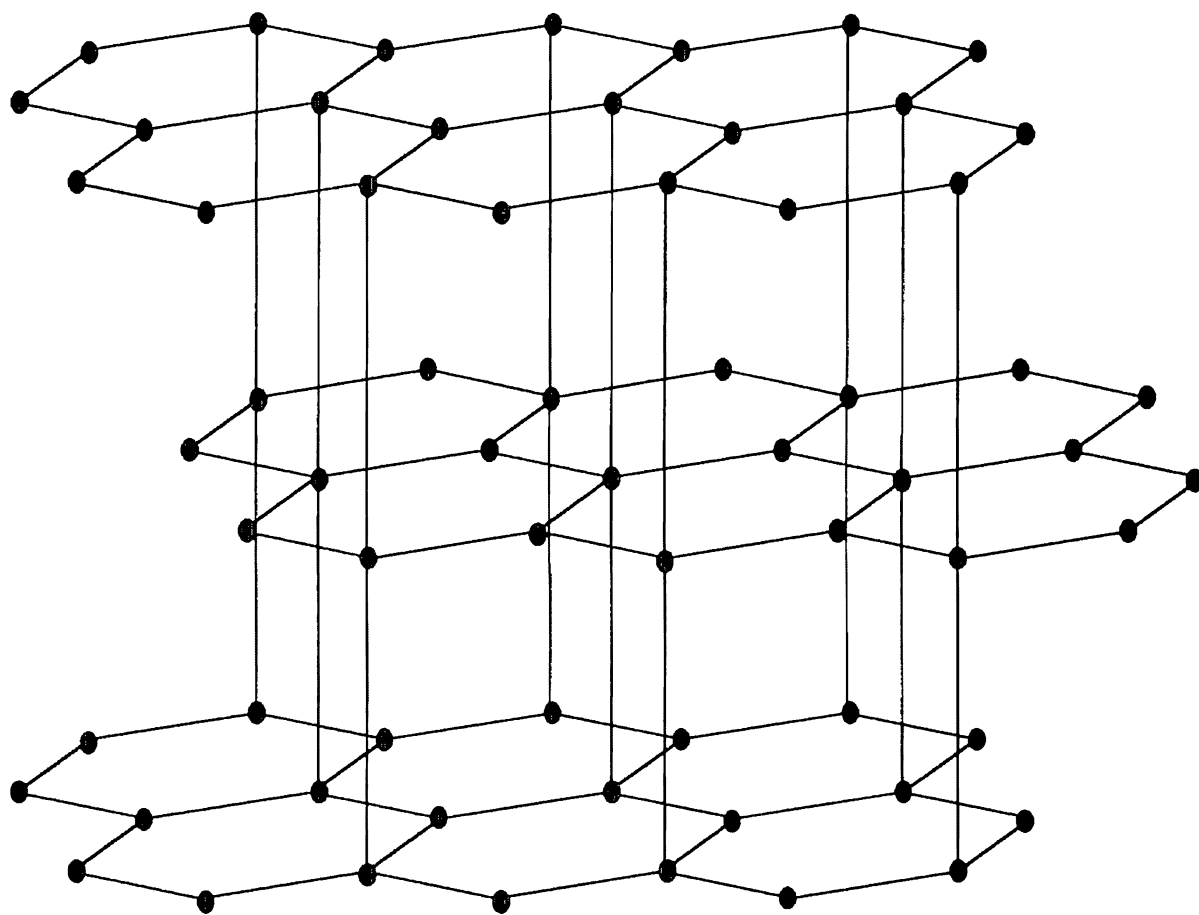


Figure 1. Structure of Graphite.

electron is engaged in a metallic-like  $\pi$  bond with an adjacent plane, weakly holding the planes together (2). Hexagonal graphite has lattice constants  $a$  and  $c$  of 2.46 Å and 6.71 Å, respectively (6). It is the long, easily broken bonds between the basal planes that give graphite its notable lubricating properties (7).

Diamond has a face-centered cubic lattice, as depicted in Figure 2, with the four valence electrons in the  $sp^3$  configuration. This corresponds to a tetrahedral coordination of the carbon atoms, where each is engaged in  $\sigma$  covalent bonding with a neighboring atom. Planes in the  $\{111\}$  direction are stacked in the ABC ABC ABC... sequence known as the "chair" configuration, where each plane consists of "puckered" six-membered rings of carbon atoms which are alternately staggered above and below the plane (7). A lattice constant of 3.56 Å and a bond length of 1.54 Å (6) give diamond a compact structure and strong chemical bonding, which attribute to its outstanding properties.

Lonsdaleite, also known as hexagonal diamond, C-2H, and "white" carbon, is a second crystallographic form of diamond (8), illustrated in Figure 3. The structural relationship between lonsdaleite and diamond is similar to that of wurtzite and sphalerite, the hexagonal and cubic forms of zinc sulfide (3). As in diamond, the four valence electrons of lonsdaleite engage in  $\sigma$  covalent bonds with neighboring atoms in the tetrahedral  $sp^3$  configuration. Likewise, planes in the  $c$ -direction are identical to the  $\{111\}$  planes of dia-

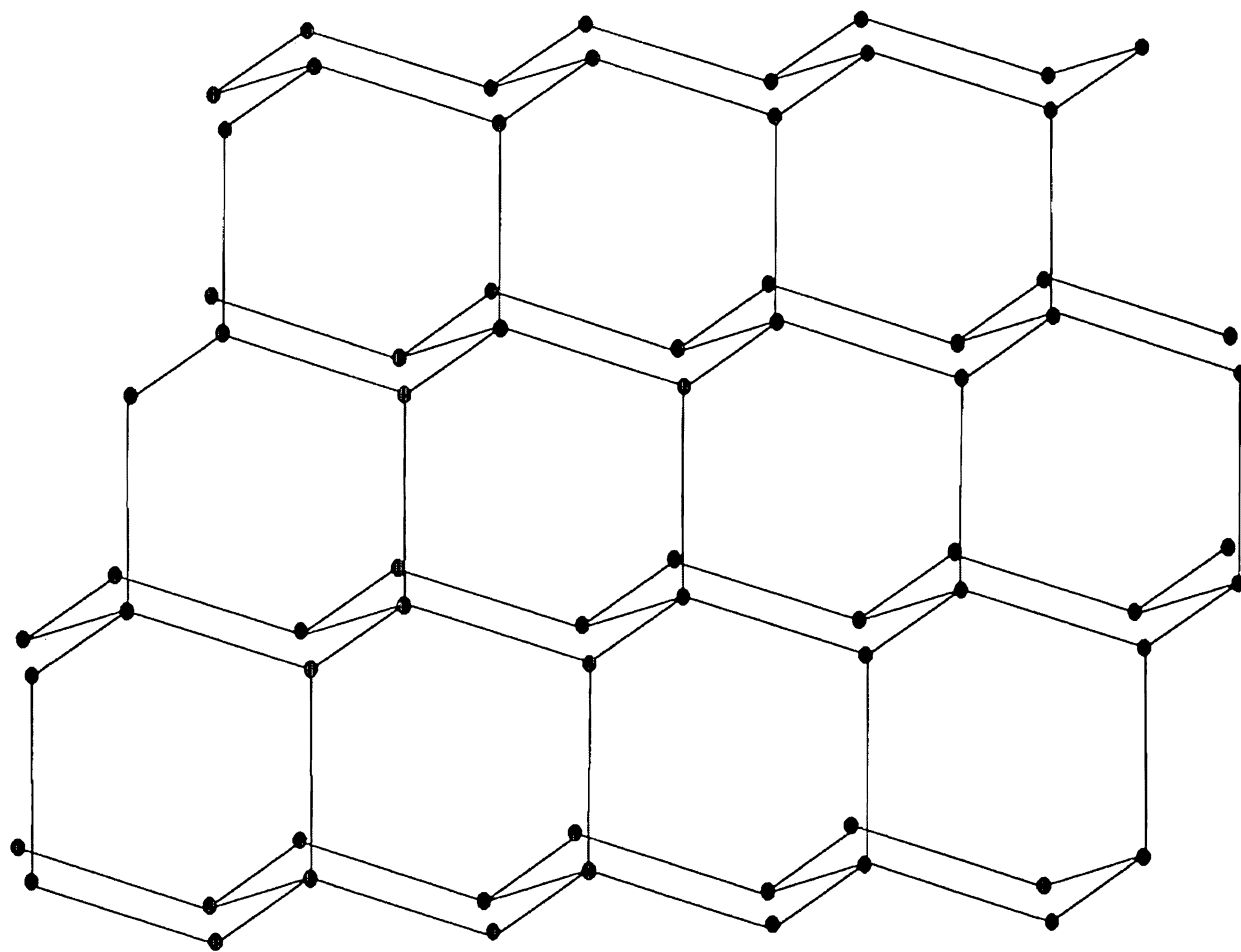


Figure 2. Structure of Diamond

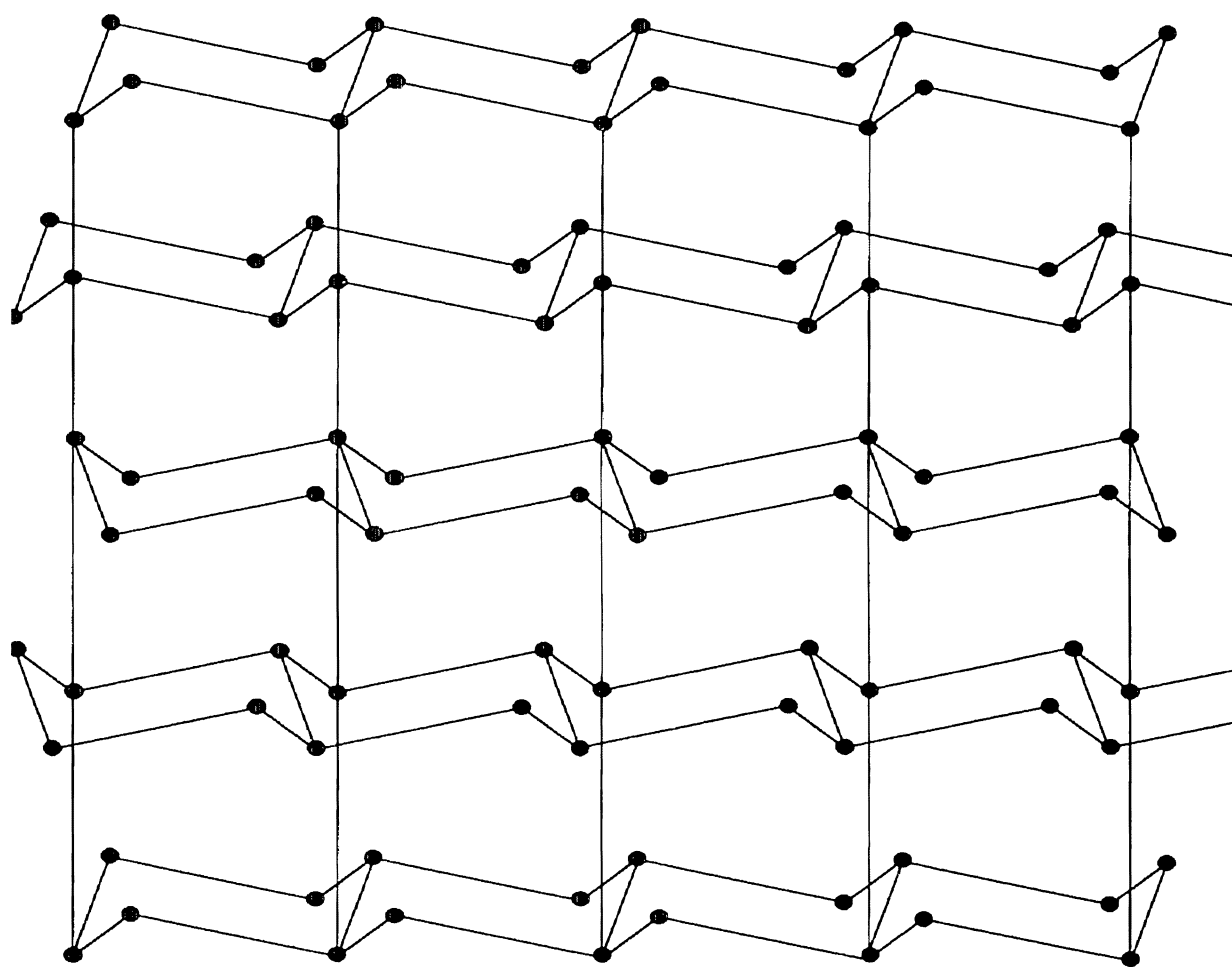


Figure 3. Structure of Lonsdaleite

mond, consisting of puckered six-membered rings which are staggered above and below the plane. In lonsdaleite, however, these planes are stacked in the AB AB AB... sequence rather than the ABC ABC ABC... sequence characteristic of cubic diamond and six-membered rings of "boats" join layers of "chairs". The difference in stacking sequences of lonsdaleite and diamond is shown in Figure 4. Lonsdaleite is birefringent and has lattice constants a and c of 2.52 Å and 4.12 Å, respectively (5). With a nearest neighbor distance of 1.52 Å, it is more closely packed than diamond. Lonsdaleite has not been found in nature, but is produced synthetically by the shock-compression of graphite (9) and has been found in meteorites (10).

Microcrystalline carbon is composed of a combination of  $sp^3$  and  $sp^2$  bonding, with only short range order. It consists of extremely small crystallites which exhibit a majority of tetrahedral  $sp^3$  bonding, but also display trigonal  $sp^2$  bonding at the grain boundaries between crystallites (7).

Amorphous carbon (a-C), like microcrystalline carbon, consists of a combination of  $sp^3$  and  $sp^2$  bonding. Amorphous carbon differs from microcrystalline carbon, however, in that it lacks long range crystalline structure. Included in the category of amorphous carbon are many types of non-crystalline carbon, which may or may not contain hydrogen (11) and may be graphitic or diamond-like, depending on whether trigonal or tetrahedral bonding is dominant. This can be

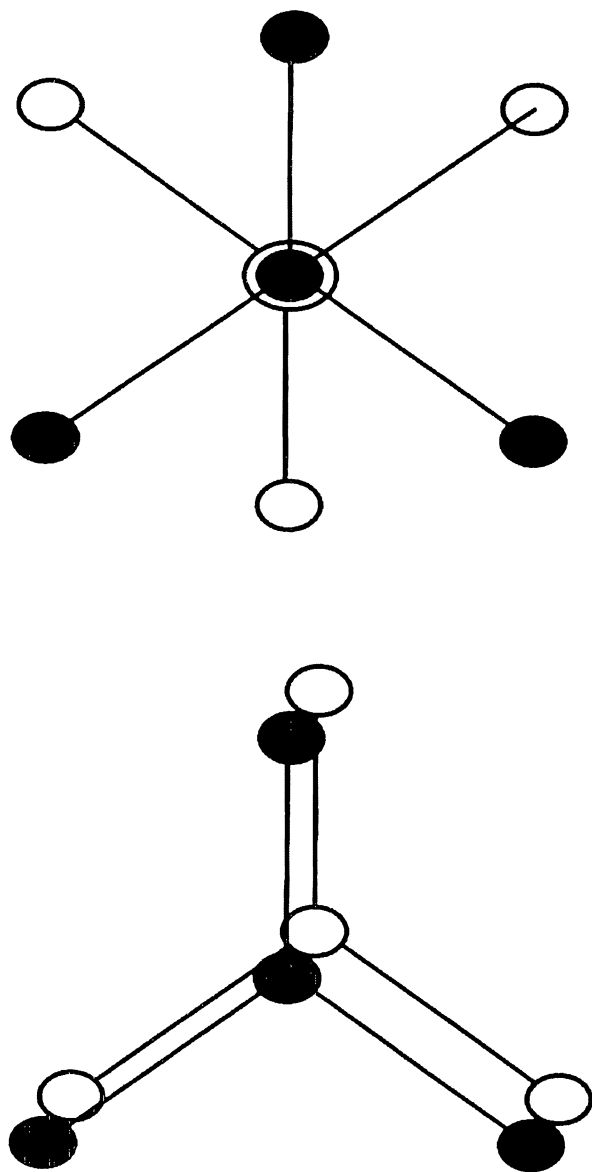


Figure 4. Stacking sequences in the  $[111]$  direction of diamond (top) and in the direction of the  $c$ -axis of lonsdaleite (bottom).

determined by the ratio of  $sp^2$  to  $sp^3$  hybridization, which is a function of the hydrogen content (2).

Diamond, graphite, microcrystalline carbon, and amorphous carbon have all been synthesized by the technique of chemical vapor deposition (CVD) in attempts to produce highly-ordered crystallized diamond. There has been no report, however, on the occurrence of lonsdaleite in these attempts. This is peculiar, since the analogous hexagonal and cubic forms of silicon carbide are both easily produced by the process of chemical vapor deposition (12).

In this study, we focus on the synthesis of well-crystallized lonsdaleite, as well as diamond, graphite, microcrystalline carbon, and amorphous carbon, using the technique of chemical vapor deposition. Raman spectroscopy was utilized to characterize the samples, giving information as to the structure, quality, and presence of internal stresses. Attempts are also made to explain what promoted the synthesis of lonsdaleite and what mechanisms were involved.



## CHAPTER 2

### REVIEW OF THE LITERATURE

#### Synthesis of Crystalline Carbon by Chemical Vapor Deposition

Chemical vapor deposition (CVD) is defined by Pierson as, "the deposition of a solid on a heated surface from a chemical reaction in the vapor phase" (2). The technique originated in the 1880's, when incandescent lamp filaments were coated with carbon or metal to improve their strength (2). Since then, the list of materials deposited by CVD has been extended to include other metallic and non-metallic materials, as well as ceramics and semiconductors. Applications include electrical, opto-electrical, mechanical and chemical functions in the form of coatings, powders, fibers, monoliths, and composites (2).

The general process of CVD involves reactions of chemical constituents in the gas phase. These reactions usually require high energy, which may be supplied by thermal means or by interaction with a plasma. A driving force, such as a temperature gradient or electric field, transports the reactants to a heated substrate where, if conditions are favorable, they will be deposited in solid form.

In the CVD of diamond and other crystalline forms of carbon, the gas phase chemical constituents must contain a

source of carbon. While methane ( $\text{CH}_4$ ) is used most frequently, acetylene ( $\text{C}_2\text{H}_2$ ), carbon monoxide ( $\text{CO}$ ), and acetone ( $\text{CH}_3\text{COCH}_3$ ), as well as a wide variety of other gases, have also been used successfully. In the CVD of diamond, hydrogen is an important constituent, because, when activated, it dissociates into atomic hydrogen, which has been found to etch graphite and stabilize the diamond structure, encouraging the synthesis of diamond over graphite (12).

Typical deposition conditions include a flow of molecular hydrogen with 0.1 to 2.0% methane, a total flow rate of 100 standard cubic centimeters per minute (sccm), a substrate temperature between 600 and 1100°C, and a pressure from 1 to 100 Torr (7). Deposition times range anywhere from 15 minutes to more than 24 hours. Studies of films at different times during the deposition have shown that the development of crystalline carbon films takes place in three stages: carbide or carbon layer formation, nucleation, and growth (13).

#### Carbide or Carbon Layer Formation

An incubation period has been observed before the onset of nucleation on many substrates. Within this period, carbide layers were found to form on carbide-forming substrates and amorphous carbon layers were found to form on other substrates (7,13,14,15,16). The process consists of initially rapid growth which drops off as the carbide or a-C layer

thickens and almost completely stops at the first appearance of diamond (13).

An interesting observation made by Williams et al. (15,16) is that different intermediate layers, i.e. carbides or a-C, can be produced on the same substrate by different gas phase compositions. The duration of the carbide or a-C formation period seems dependent on the carbon diffusion rate of the substrate, which is directly related to the carbon surface saturation. The process appears to continue until a critical surface carbon concentration is attained, which is necessary for the formation and survival of stable nuclei.

### Nucleation

Nucleation occurs with the formation of nuclei of a critical size, large enough that the contributions between volume and surface energies will balance (17). In agreement with thermodynamics, the free energy of the reaction must be negative for the process to occur. The contribution of bond formations between atoms in a nucleus is negative, while the corresponding contribution of the surface, due to bond strains and unsatisfied valencies is positive (7). Thus, until the nuclei reach their critical size, they will be unstable.

Matsumoto (18) has suggested that  $sp^3$  bonded multiply-twinned hydrocarbon cage compounds with six-membered carbon rings, like adamantane, tetracyclododecane, and hexacyclo-

pentadecane, could function as nuclei (7). These compounds are not normally stable at typical diamond CVD temperatures, but may be stabilized by the supersaturation of carbon and atomic hydrogen long enough to form critical nuclei (7). Those nuclei that do not obtain critical size are absorbed by other nuclei or dissociate. The presence of hydrogen cage compounds could explain the repeated occurrence of multiply-twinned crystals at the diamond/substrate interface, as is supported by Figure 5.

The nucleation of diamond on substrate surfaces may be enhanced by scratching, carbon coating, and seeding with diamond particles (14). Scratching with diamond or other abrasives has been found to increase the number of nucleation sites on a sample, either by leaving a residue of diamond or other carbon particles, which act as seeds, or by mechanically damaging the sample, creating high energy damage sites on the surface (19). Covering the substrate with carbon-containing species, such as amorphous carbon (14) or even pump oil (20), also enhances nucleation, either by saturating the surface with carbon (14), or by reducing stress by improving the lattice match (7). In seeding the substrate, subsequential nucleation just involves the growth of new diamond on the already existing seed (19).

The nucleation rate and nucleation density depend not only on the surface treatment, but also on deposition parameters. Kim et al. (21) have determined that the nucleation rate increases as the methane concentration is increased

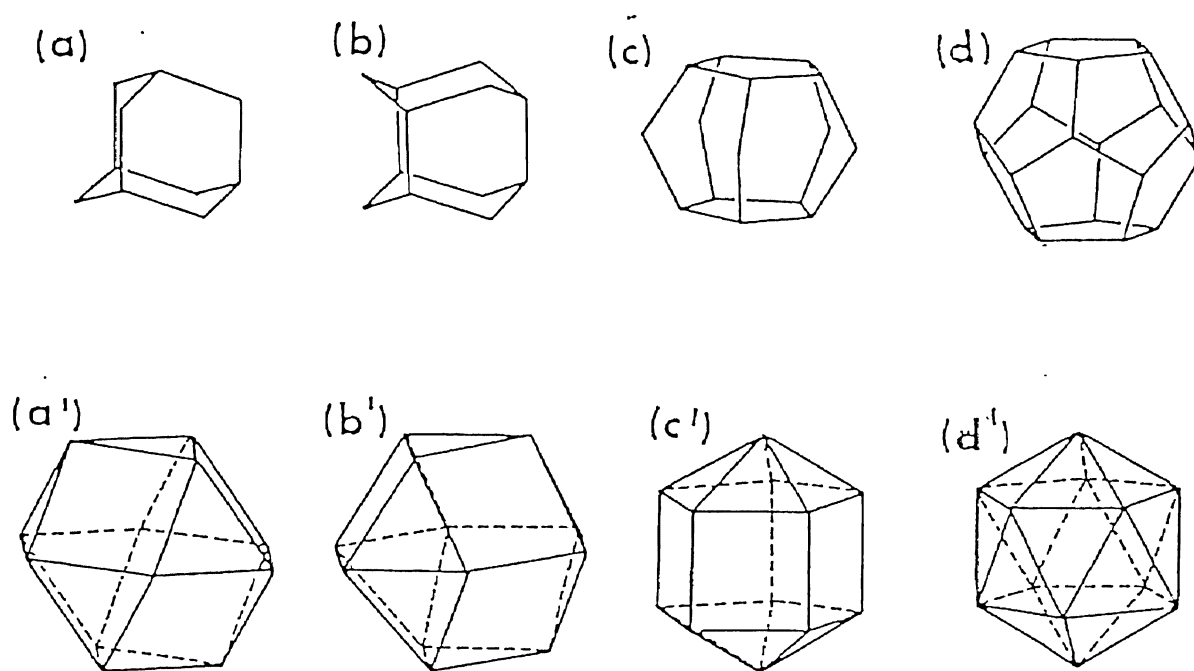


Figure 5. Hydrocarbon Cage Compounds Proposed as Nuclei (a = adamantane, b = tetra-cyclo[4.4.0.1.1]dodecane, c = hexacyclo[5.5.1.1.1.0.0]pentadecane, d = dodecahedrane) and Associated Twinned Diamond Particles (a' = cubo-octahedron, b' = twinned cubo-octahedron, c' = decahedral Wulff polyhedron, d' = icosahedron)(from Reference 7)

from 0.3 to 1.5% and as the substrate temperature approaches 900 to 1000°C from either side. Chang et al. (22) have determined that the nucleation density increases as the pressure is decreased from 20 to 2 Torr and as the flow rate is increased. In the method of filament-assisted CVD, the filament condition may also affect the nucleation rate. In the first thirty minutes of use of a new filament, most of the carbon in the system goes into the carburization of the filament, thus lowering the nucleation rate at the substrate by reducing the surface carbon concentration (7).

When the nucleation rate is increased, a greater number of planar defects and graphitic and amorphous inclusions are generated. When the nucleation density is increased, the nucleation rate will decrease (13) and smaller grains will be grown during the same deposition time (14). In any event, the nucleation density will increase with time from the beginning of the deposition until a saturation level is reached (14).

### Growth

Once the saturation level of nucleation is reached, the stable nuclei on the substrate coarsen and become more faceted, often exhibiting a preferred orientation (23). According to Kim et al. (24), this orientation is related to the ratio of the total surface energy to the volume. The lowest ratio is for octahedra, which are composed of (111) crystallographic planes (24). As growth progresses, the

most important quantity becomes the surface area to volume ratio, which is lowest for cubo-octahedra. Thus, octahedra grow into cubo-octahedra. The growth rate of both octahedral and cubo-octahedral faces is determined by the combined growth rates of the (100) and (110) faces.

The morphology, growth rate, and crystalline structure of the films were greatly affected by changes in the methane concentration, flow rate, and substrate temperature. For methane concentrations increasing from 0.2 to 2%, (111) faces shifted to (100) faces (12). For 2 to 6% methane, (100) faces prevailed, with the smoothest (100) faces at 6% (12,25). For methane concentrations greater than 7%, the films became microcrystalline (25). The growth rate increased with methane concentration up to 5%, and then decreased for higher concentrations (25). The initial increase in growth was more than likely due to an increase in the carbon concentration of the gas phase and the decrease caused by  $sp^2$  carbon formation, which inhibited the growth of diamond (25).

The relationship between methane concentration and crystalline structure was determined in a study by Zhu et al. (26). No graphite or other non-diamond components were found at a methane concentration of 0.5%, while a methane concentration of 2% produced highly oriented graphite crystallites on or near the {111} diamond planes. At 5% methane, graphite crystallites were randomly distributed and as the methane concentration increased, so did the density of

defects like stacking faults and twins on the {111} diamond planes.

The flow rate of the reactants has been found by Celii et al. (20) to strongly affect orientation and film quality. At flow rates of 100 and 200 sccm, dominant (100) and (111) facets were grown on silicon, respectively. Diamond films grown on a layer of microcrystalline diamond had dominant (100) facets at 100 sccm, but at other flow rates appeared to have only random distributions. On some occasions, films displayed small pyramidal grains, indicative of growth on the (110) plane. The highest quality films were produced at 400 sccm on silicon and at 100 sccm on microcrystalline diamond. The dependence of morphology and quality on flow rate may actually be dependent on the gas residence time, either in changing the gas phase reactant concentration, or by changing the surface reaction time.

There is a narrow range of temperature over which single-phase diamond will grow, according to Yarbrough (12) and Badzian (17). At temperatures less than 800°C, a large amount of a-C is co-deposited, while temperatures over 1100°C promote the growth of non-diamond components, including graphite and microcrystalline carbon. In both instances, only fine grained films with no distinguishable faceting are found (12). Meiluras (27) and Badzian (17) report 1000°C as the temperature of best crystal quality and highest growth rate, respectively, although the optimum nucleation temperature is 925°C. At the higher and lower ends



of the optimum temperature range, films display highly-faceted cubic and octahedral surfaces, respectively (17).

In studying the growth of diamond films, it is helpful to know what constituents are present and what roles they play. When activated by a filament or plasma,  $H_2$  molecules decompose into atomic hydrogen while methane is dehydrogenated to  $CH_3$ ,  $CH_2$ , and  $CH$  radicals. The atomic hydrogen has been found to decompose hydrocarbon radicals, etch graphite at 20 times the rate it etches diamond (7), and stabilize  $sp^3$  bonds on the diamond plane. Without hydrogen, it is believed that the {111} diamond planes would collapse to flat basal planes of graphite (7). The products resulting from the dehydrogenation of methane provide the carbon necessary for diamond growth.

Several studies have been undertaken to determine the growth mechanisms involved in the synthesis of diamond by CVD. The principal species detected in hydrogen/methane ( $H_2/CH_4$ ) environments by both in situ and ex situ analysis are molecular and atomic hydrogen ( $H_2$  and  $H^+$ , respectively), methane ( $CH_4$ ), methyl radicals ( $CH_3^+$ ), acetylene ( $C_2H_2$ ), and ethylene ( $C_2H_4$ ), although ethane ( $C_2H_6$ ),  $C_2H$ , and hydrocarbons with three or more carbons have also been detected (7). Kinetic models have confirmed the major species present and suggest that the dominant carbon growth species could be  $CH_4$ ,  $CH_3^+$ ,  $C_2H_2$ , and/or  $C_2H_4$  (7).

A growth mechanism employing atomic hydrogen and a hydrocarbon species has been proposed by Frenklash and Spear

(28). This model, which assumes that diamond growth occurs mainly from  $C_2H_2$  and  $CH_3^+$ , is displayed in Figure 6. The proposed mechanism assumes a reaction between the atomic hydrogen bound to the diamond surface and acetylene in the gas phase, whereby hydrogen ions bound to the diamond surface are first removed by atomic hydrogen, and then a hydrocarbon species -- in this case acetylene, is added to the diamond surface.

The addition of oxygen to the CVD system was found to increase the quality and growth rate of diamond films by reducing the concentration of unsaturated hydrocarbons, like  $C_2H_2$  (29,30). As a result, the deposition of graphitic or a-C is suppressed, since the concentration of  $C_2H_2$  is strongly related to their formation (30). The rate of diamond growth increases with the addition of oxygen, because the total number of methyl radicals can be increased by increasing the flow rate or pressure (30). Studies by Uchida et al. (31,32) have additionally determined that oxygen has a stronger etching effect than hydrogen and, although it also attacks diamond, is still rather selective.

#### Failure to Produce Lonsdaleite

Although diamond, graphite, microcrystalline carbon, and a-C have all been produced by CVD methods known to produce well-crystallized diamond, the production of lonsdaleite has never been reported. Several papers have reported on the synthesis of hexagonal polytypes, including the 6H polytype

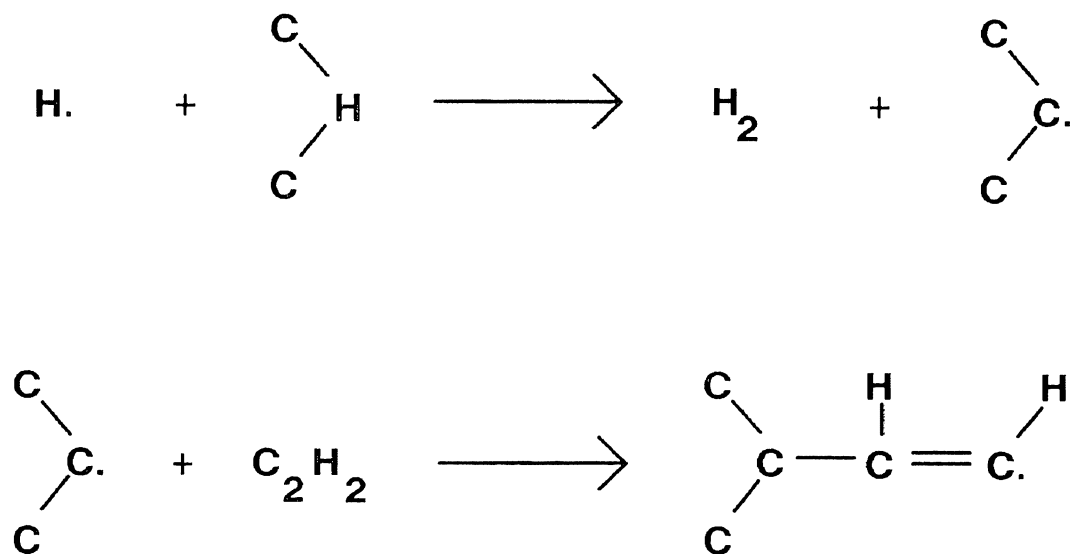


Figure 6. Proposed Model of the Growth Mechanism of Diamond: the removal of a surface bonded hydrogen ion by atomic hydrogen (top), followed by the reaction of a surface carbon radical with a hydrocarbon species in the gas phase (bottom)

(3) and possibly a combination of the 12H and 20H polytypes (4), although the films were of poor quality. Not much more will be said about these polytypes except that they are composed of varying amounts of hexagonal and cubic tetrahedral layers arranged in various sequences. The 6H polytype, for example, consists of one hexagonal layer followed by two cubic layers (3).

According to Frondel and Marvin (33), there should be a range of diamond structures similar to those of silicon carbide. This opinion is based on the fact that the cubic and hexagonal polytypes of diamond are closely related to the hexagonal and cubic polytypes of silicon carbide and that 65 distinct hexagonal and rhombohedral silicon carbide structures have been synthesized by stacking varying amounts of hexagonal and cubic tetrahedral layers (3). The hexagonal and cubic polymorphs of silicon carbide are made easily using a technique of CVD similar to that of diamond.

Another argument makes note of the  $sp^3$  bonded multiply-twinned hydrocarbon cage compounds which are believed to function as nuclei in the nucleation process. The six-membered carbon rings in these molecules consist of either the "chair" form, "boat" form, or a combination of the two. The combination of "chair" and "boat" configurations suggests the potential for the nucleation of both diamond and lonsdaleite. Despite this argument, only the frequent twinning of the crystals across the (111) planes has been observed (12).

There is only one explanation as to why growth conditions might not be favorable for lonsdaleite. The "boat" configuration is known to be less stable than the "chair" configuration because of the perfect eclipsing of  $sp^3$  bonds along two of the C-C bonds needed to form the six-membered ring (12). As a result, lonsdaleite may be less stable than either diamond or graphite. The frequent formation of the twin planes, which are believed to be conducive to the growth of either diamond or lonsdaleite, is explained by small energy differences between the formations of the "chair" and "boat" forms of the six-membered hydrocarbon cage compounds.

## CHAPTER 3

### SAMPLE PRODUCTION

#### Experimental Apparatus

In the present experiment, the method of filament-assisted CVD was chosen for sample production, because of its reasonably low operational cost and large deposition area. The experimental CVD apparatus used in this experiment is shown schematically in Figure 7.

The deposition chamber consisted of a silica glass cylinder twelve inches high with a six inch inner diameter and three-quarter inch thick walls. A tungsten filament was clamped to two large copper electrodes which were connected to a step-down transformer, ammeter, and variac voltage regulator. The stainless steel substrate holder consisted of two clamps which touched only the corners of the sample. It was suspended from the top plate and was adjustable, so that the distance between the filament and substrate could be varied. Feed gases traveled from tanks to flow meters and into an external mixing chamber before being fed into the bottom of the deposition chamber where they were aimed at the filament. A Leibold model 4-A Rotary Pump was connected to the deposition chamber by way of valves on both the top and bottom plates. The lower opening measured three

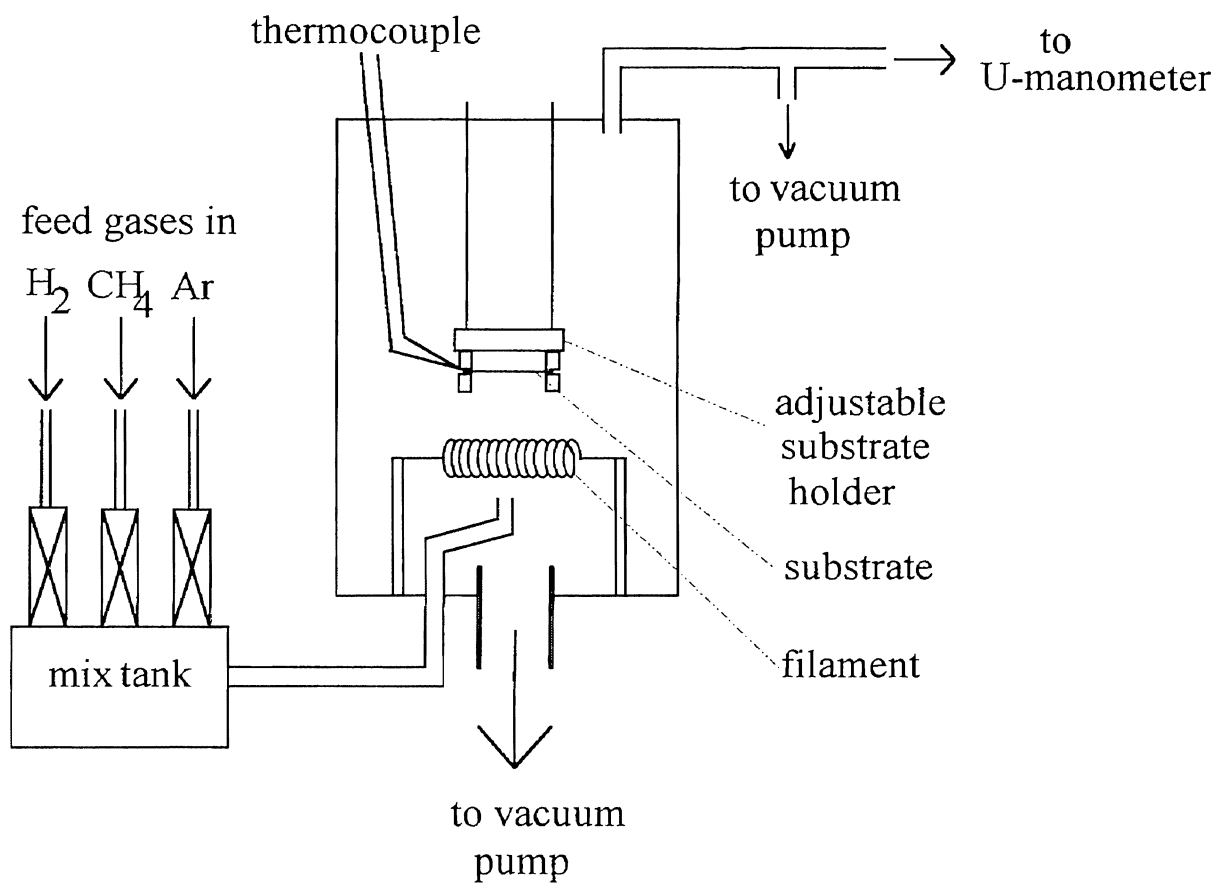


Figure 7. Experimental Filament-Assisted Chemical Vapor Deposition Apparatus Used for Sample Production

inches across and was used solely for the purpose of pumping out large quantities of gas. The upper opening was one half inch in diameter and could be controlled more accurately than the large opening. It was thus used during deposition to match the gas flow out of the chamber with the flow going in. The substrate temperature was measured with a tungsten/3% rhenium vs. tungsten/25% rhenium thermocouple held to the substrate by a silicon backing. The filament temperature was measured with a three-band optical pyrometer focused on the hottest area of the filament. Pressure was measured with a U-manometer connected to the top plate of the deposition chamber.

#### Procedure

Substrates were cut to roughly 2 cm x 2 cm from four inch polished silicon wafers obtained from Wacker. The wafers had {100} orientation and were all from the same lot. After being cut, substrates were scratched with nine micron and one micron diamond polish, respectively, rinsed, and then cleaned with acetone.

The substrate was secured to the substrate holder with the thermocouple sandwiched between it and the silicon backing. The top plate was then put into place and the substrate-to-filament distance was adjusted to approximately five millimeters. The deposition chamber was evacuated to roughly  $10^{-2}$  Torr, closed off and filled with argon to approximately 100 Torr. It was then pumped down again. This



procedure was followed in order to remove a larger percentage of air, since much of the air left from the first time is replaced with argon in the second pumping.

The filament was turned up to its full operating power in one step. The substrate and substrate holder, having a minimal amount of mass, quickly reached an equilibrium temperature. The vacuum valve was then closed and the hydrogen/methane mixture was allowed in. When the desired pressure was reached, the top plate vacuum valve was opened slightly and adjusted until the hydrogen/methane mixture was pumped out at the same rate at which it was supplied.

The system was monitored every ten to thirty minutes for the entire deposition period - which ranged from three to four hours. At the end of this period, the gases were turned off, the bottom plate valve was opened fully, and the filament was shut off, in that order. The system was maintained at approximately  $10^{-2}$  Torr until the substrate had cooled to room temperature. It was then removed and was ready for characterization.

## CHAPTER 4

### RAMAN SPECTROSCOPY

#### Theory

The Raman process was first predicted from theoretical considerations by A Smekal in 1923 and was discovered by C. V. Raman five years later (34). The effect is described as an inelastic, non-resonant light scattering process in which an incident photon, or light quanta, interacts with matter. The result is the emission of a photon of different frequency than the incident photon and either the creation or annihilation of a phonon, or quanta of lattice vibration.

When a sample is irradiated with monochromatic radiation, a small portion of the incident radiation will be scattered from the main direction of propagation. The largest percentage of this represents Tyndall scattering, caused by dust particles or inhomogeneities in the sample (34). Rayleigh scattering is also present, which is caused by the polarizability of the scattering medium (34). These types of scattering are considered elastic, since the radiation is scattered at the same frequency as that of the source.

Inelastic Raman scattering is considerably weaker than Tyndall or Rayleigh scattering. It is caused by changes in the polarizability of the sample. Raman scattering is con-

sidered inelastic because the scattered radiation is of a different frequency than that of the source. The intensity of the scattered light is extremely weak -- approximately  $10^{-8}$  times the intensity of the source (34).

It is important to note that most absorption or emission spectroscopy involves scattering in which the radiation is in resonance with the energy level transition of the material. Raman spectroscopy, however, is due to the scattering of non-resonant absorption or emission, and it is the frequency shift that gives information about the energy level transitions. In Raman scattering, the scattered photon brings extra information away with it, including information on rotational and vibrational transitions of the material (34).

### Basic Theory

Monochromatic radiation is composed of discrete, quantized packets called photons. Each photon has energy  $E = h\nu$ , where  $h$  is Planck's constant and  $\nu$  is the frequency of the radiation. When light passes through materials, scattering occurs as incident photons are absorbed by molecules and new photons are subsequently re-emitted.

In the Raman effect, a photon with initial energy  $h\nu_0$  interacts with a molecule, resulting in the scattering of a photon of energy  $h\nu_s \neq h\nu_0$  and the creation or annihilation of a phonon. The Raman effect must follow the law of conservation of energy, so that in a Stokes transition, where

$h\nu_S < h\nu_O$ , a phonon of energy  $h\nu_O - h\nu_S = h\nu$  is created. Likewise, in an anti-Stokes transition, where  $h\nu_S > h\nu_O$ , a phonon of energy  $h\nu_S - h\nu_O = h\nu$  is annihilated. Thus, the Raman effect follows the selection rule

$$\nu_O = \nu_S \pm \nu \quad (2-1)$$

where  $\nu_O$ ,  $\nu_S$ , and  $\nu$  refer to the frequencies of the incident photon, scattered photon, and phonon, respectively. If there is no such phonon with energy  $h\nu$ , then the corresponding transition from  $h\nu_O$  to  $h\nu_S$  is forbidden.

### Polarizability Theory

Electromagnetic radiation travels in waves which consist of an oscillating electric field and an oscillating magnetic field perpendicular to the direction of propagation and perpendicular to each other. The electromagnetic wave contains no charge, but transfers energy from one oscillating dipole within a medium to another. When the wave arrives at a medium, it sets up an oscillating electric dipole within the material which radiates at the frequency of oscillation (34). The applied field and the induced dipole moment are related according to the equation

$$\mathbf{M} = \alpha\mathbf{E} = \alpha\mathbf{E}_O \cos(2\pi\nu_O t) \quad (2-2)$$

where  $\mathbf{M}$  is the induced dipole moment,  $\mathbf{E} = \mathbf{E}_O \cos(2\pi\nu_O t)$  is the applied field, and  $\alpha$  is the polarizability (35). In a crystal, the atoms are ordered, resulting in normal modes of oscillation. The atoms move with periodic motion and the polarizability, which varies harmonically, is of the form

$$\alpha = \alpha_0 + \alpha_1 \cos(2\pi\nu t) \quad (2-3)$$

where  $\alpha_0$  is the polarization of the atoms at equilibrium,  $\alpha_1$  is the amplitude of the additional polarizability due to vibrations, and  $2\pi\nu$  is the angular vibrational frequency (35). Thus,

$$\mathbf{M} = [\alpha_0 + \alpha_1 \cos(2\pi\nu t)] \mathbf{E}_0 \cos(2\pi\nu_0 t) \quad (2-4)$$

or, using the trigonometric identity

$$\cos a * \cos b = \frac{1}{2} [\cos(a+b) + \cos(a-b)],$$

this is equivalent to :

$$\begin{aligned} \mathbf{M} = \alpha_0 \mathbf{E}_0 \cos(2\pi\nu_0 t) + \frac{1}{2} \alpha_1 \mathbf{E}_0 [ & \cos(2\pi(\nu_0 + \nu)t) \\ & + \cos(2\pi(\nu_0 - \nu)t) ] \end{aligned} \quad (2-5).$$

The induced electric dipole moment is thus the superposition of three periodically changing moments, the frequencies of which are  $\nu_0$ ,  $(\nu_0 + \nu)$ , and  $(\nu_0 - \nu)$ . These frequencies represent elastic Rayleigh and inelastic anti-Stokes and Stokes scattering, respectively.

In the case of an asymmetrical molecule, the induced dipole moment does not have to point in the same direction as the electric field. The x, y, and z components of the induced dipole moment are given by

$$\begin{aligned} M_x &= \alpha_{xx} E_x + \alpha_{xy} E_y + \alpha_{xz} E_z \\ M_y &= \alpha_{yx} E_x + \alpha_{yy} E_y + \alpha_{yz} E_z \\ M_z &= \alpha_{zx} E_x + \alpha_{zy} E_y + \alpha_{zz} E_z \end{aligned} \quad (2-6)$$

where the  $\alpha_{ij}$ 's are the components of the polarizability tensor and  $\alpha_{xy} = \alpha_{yx}$ ,  $\alpha_{xz} = \alpha_{zx}$ ,  $\alpha_{yz} = \alpha_{zy}$  (35). If one or more of the six  $\alpha_{ij}$ 's is non-zero, the Raman transition is allowed.

Rotational Raman lines will occur when spherically asymmetric molecules rotate. The scattered radiation will contain the sums and differences of the frequency of incident light and the frequency of rotation. This is a result of the anisotropic part of the polarizability (35). The rotational frequencies have a much smaller order of magnitude than vibrational frequencies and appear as satellites on the exciting line of the incident radiation (35).

Vibrational Raman lines will occur when the atoms in a molecule vibrate, appearing as distinct lines displaced from the exciting line by large frequency shifts (35). The Raman scattering in this case will consist of sums and differences of the incident radiation and the frequency of molecular vibration. If the vibrations are purely harmonic, each vibration will independently contribute to the induced dipole moment (35). In reality the vibrations are not strictly harmonic and higher terms than quadratic must be included in the potential energy function, so that the vibrational energy contains cross terms of two or more normal vibrations (35).

#### Experimental Apparatus

The light scattering set up of the Raman spectrometer used in this experiment is shown schematically in Figure 8. A Spectra Physics model 2020 Argon-Ion laser was used to produce monochromatic light of wavelength 5145 Å. The power of the laser was variable, from roughly 200 to 500 mW.

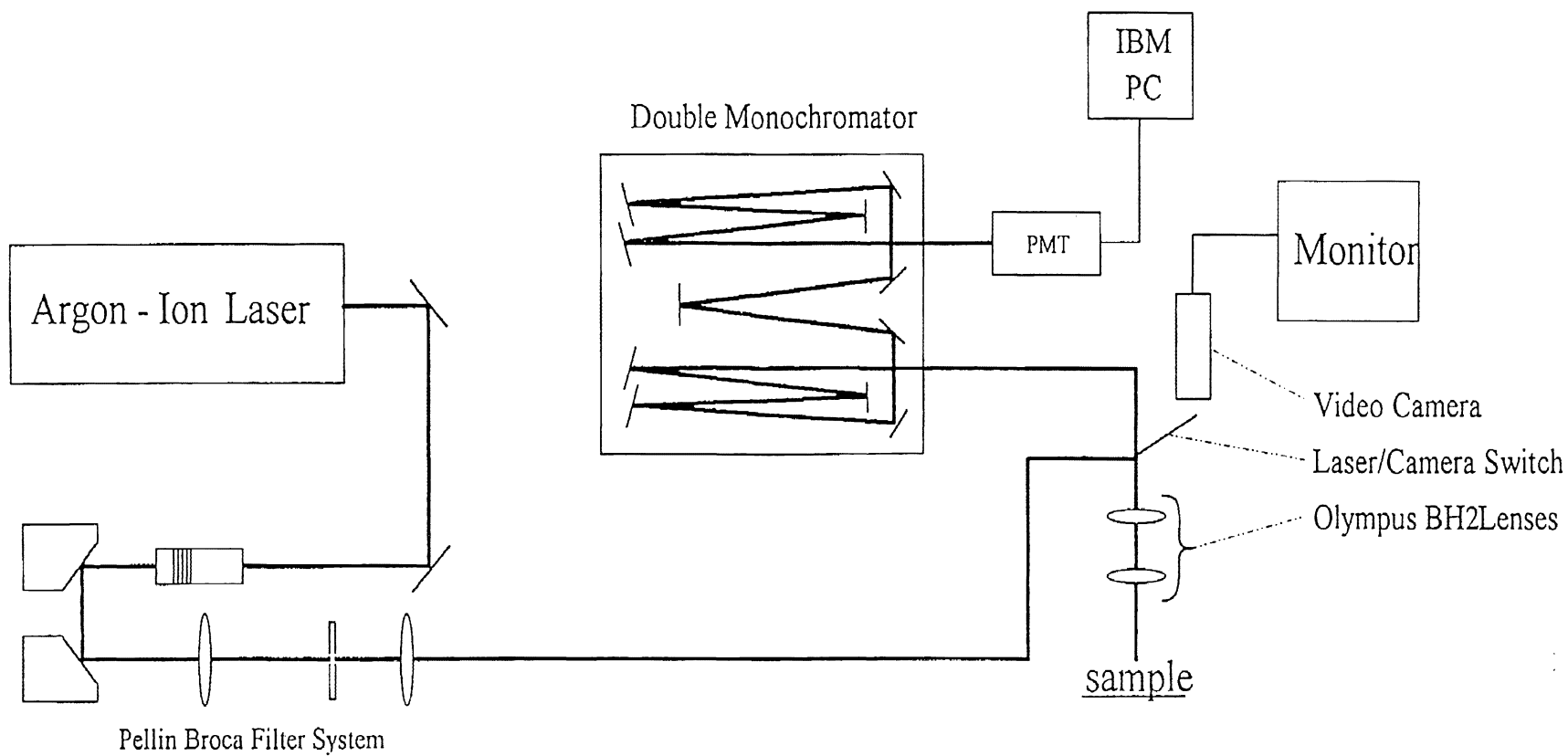


Figure 8. Experimental Apparatus for Raman Spectroscopy

The laser output was directed into a Pellin Broca filter system, which allowed the selective transmission of vertically polarized light. Prisms in the system filtered the non-lasing plasma lines by dispersing the light. It was then re-focused by a lens of focal length 300 mm and directed through a pinhole aperture placed 300 mm away. From there, it entered a second lens located 100 mm away, with focal length 100 mm, and was directed into an Olympus BH2 metallurgical microscope by a system of mirrors.

The Olympus BH2 is equipped with an eyepiece of magnification 10X. Objectives of magnifications 10X, 50X, and 100X are mounted on a rotatable turret, giving total magnifications of 100X, 500X, and 1000X, respectively. Incident laser light is focused on samples at an angle perpendicular to the sample surface through the Olympus BH2 lens system.

Scattered light was collected in the back scattering configuration, focusing into a Jobin-Yvon Ramanor U-1000 double monochromator. Each monochromator features an asymmetric Czerny-Turner mounting with two symmetrical opening slits. The two diffraction gratings (1800 grooves/mm) rotate on a horizontal shaft parallel to the grating grooves. A concave mirror of focal length 0.5m couples the two monochromators by imaging the exit slit of the first with the entrance slit of the second. Four mirrors, all with focal length 1m, divert the optical paths.

Light exiting the double monochromator was directed into an RCA C31034A photomultiplier tube (PMT) which was cooled



to  $-20^{\circ}\text{C}$  using a Products for Research thermoelectric cooling unit. The PMT was in turn connected to an IBM PC with Enhanced Prism software, used for scanning and analysis. Scans were printed out using a Hewlett-Packard plotter connected to the IBM PC.

### Procedure

Each day the Raman spectrometer was used, calibration procedures were performed. Within the double monochromator, the mirror coupling the two monochromators and the concave mirror nearest to the exit slit were adjusted to maximize the signal intensity. This was done using the known  $1122.8\text{ cm}^{-1}$  peak produced by the 5461 Å mercury line of room light. Calibration was double checked using silicon and single-crystal diamond samples in the microscope, which have known peaks at  $520.0\text{ cm}^{-1}$  and  $1332.5\text{ cm}^{-1}$ , respectively.

Samples were placed under the microscope and differences in grain size, orientation, color, and density were noted as a function of region using objectives of 10X, 50X, and 100X, so that detailed maps could be drawn showing the different regions. Each region was then analyzed using the most practical objective lens: 10X for larger areas, showing general trends within a region, 50X for the study of clumps of grains, and 100X for analysis of individual grains.

Each area to be analyzed was first scanned from  $500\text{ cm}^{-1}$  to  $1600\text{ cm}^{-1}$ , with an increment of  $1.5\text{ cm}^{-1}$  and an integration time of 0.2 seconds. The power of the laser was set at

500 mW whenever possible, but when this vaporized the sample, lower powers of 200 to 300 mW had to be used. Peaks of interest were scanned over a narrower range of wavenumbers with a smaller increment and a longer integration time, resulting in increased accuracy. Enhanced Prism software was used to determine the positions of peaks and their full widths at half the maximum of the peak heights (FWHM). All scans were saved on the IBM PC hard drive and could be plotted out or examined at a later time.

## CHAPTER 5

### EXPERIMENTAL RESULTS AND ANALYSIS

Samples were produced with methane concentrations and total gas flow rates greater than those values typically used in CVD diamond production. Previous studies have reported that higher methane concentrations resulted in an increase in defects, while higher flow rates promoted the random orientation of crystals. As a result, variations in the parameters of methane concentration and total flow rate were deemed most likely to produce lonsdaleite and other non-diamond forms of carbon. Table I summarizes the growth parameters for each sample included in this study, while a graph of the flow rate plotted against the methane concentration for each sample is shown in Figure 9.

#### Reported Raman Signatures of the Allotropes of Carbon

Raman scans, taken in the different regions of each sample, were compared to the Raman spectra of the crystalline forms of carbon. Since lonsdaleite, diamond, graphite, and the other allotropes of carbon all have unique structures, each also has its own "trademark" Raman signature, so that peak positions distinctly specify what forms of carbon are present. The FWHM values determine the crystal quality,

TABLE I

SUMMARY OF CHEMICAL VAPOR DEPOSITION GROWTH PARAMETERS  
FOR ALL SAMPLES

Sample Number	%CH <sub>4</sub>	Flow Rate (sccm)	Substrate Temperature (°C)	Pressure (Torr)	Deposition Time (hours)
1	3	500	785	31	4
2	1.5	450	880	30	3.5
3	2	250	940	26	3
4	3	100	966	17	4
5	4	175	900	31	3
6	5	200	860	33	3

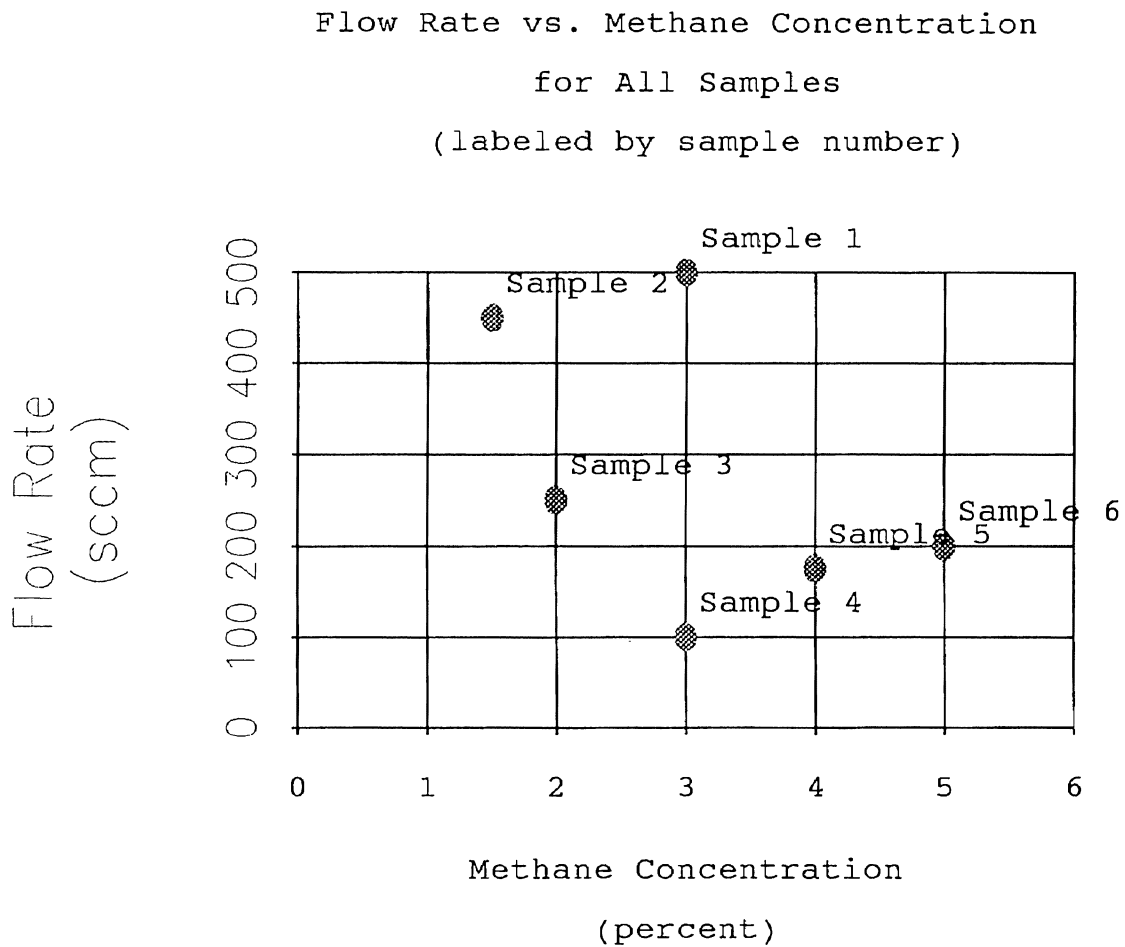


Figure 9. Graph of Flow Rate versus Methane Concentration for All Samples, Labeled by Sample Number.

since it is the crystal structure which gives rise to the Raman effect. Previous studies by Bonnot (8), Schroeder et al. (36), and Buckley et al. (37) include information on peak positions and FWHM values for many of the allotropes of carbon. Table II summarizes the reported peak positions and widths of the crystalline forms of carbon relevant in this study.

The Raman spectrum of natural diamond, shown in Figure 10, has a first-order peak at 1332.5, due to its fourfold coordinated  $sp^3$  bonding and has a width of roughly 2  $cm^{-1}$ . Naturally occurring diamond contains only 1.1%  $^{13}C$ , although synthetic diamond may be doped with varying percentages of the isotope. With a 15%  $^{13}C$  concentration, the first-order diamond peak shifts to 1328  $cm^{-1}$ , and with a 36%  $^{13}C$  concentration, the peak is shifted to 1318.6  $cm^{-1}$ .

The Raman spectra of shock-induced high pressure lonsdaleite powder displays a broad peak centered in the range of 1315 to 1326  $cm^{-1}$ , with a FWHM value of 30  $cm^{-1}$ . In another study, done by Knight et al. (38), lonsdaleite was reported to produce a sharp peak at 1319  $cm^{-1}$  with a width of 2.2  $cm^{-1}$ . In this study, lonsdaleite was thought to have formed on the the sawed surface of a ballas diamond due to shear stresses present in the cutting process.

Perfect graphite is reported to have a first-order Raman peak at 1578  $cm^{-1}$ , due to in-plane displacements of strongly coupled atoms in the basal planes. A typical Raman spectrum

TABLE II

SUMMARY OF REPORTED RAMAN PEAK POSITIONS AND PEAK WIDTHS  
FOR VARIOUS ALLOTROPIC FORMS OF CARBON

Form of Carbon	Peak Position(s) ( $\text{cm}^{-1}$ )	Peak Width(s) ( $\text{cm}^{-1}$ )
natural diamond	1332.5	2
diamond with 15% $^{13}\text{C}$	1328	2
diamond with 36% $^{13}\text{C}$	1319	2
ballas-sawed lonsdaleite	1319	2.2
shock-induced lonsdaleite	1316 to 1325	30
graphite	1578	20
microcrystalline carbon	1580, 1350	both broad
amorphous carbon	1540	very broad
diamond-like amorphous carbon	1540, 1300 to 1350	both very broad

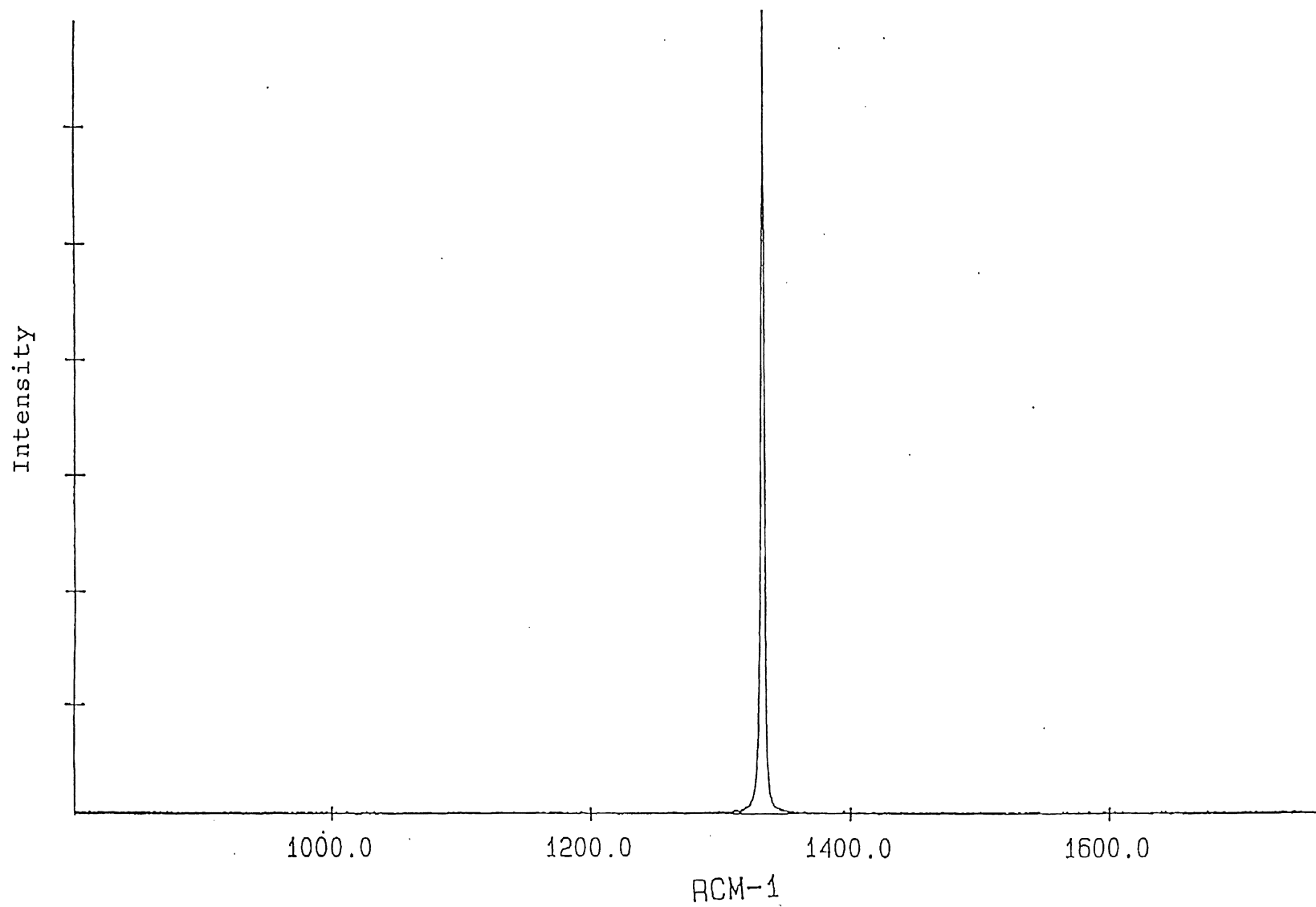


Figure 10. Typical Raman Spectrum of Natural Diamond



for graphite is shown in Figure 11. The FWHM value of graphite is reported to be approximately  $20 \text{ cm}^{-1}$ . The Raman spectrum of microcrystalline graphite is composed of two broad bands at  $1580$  and  $1350 \text{ cm}^{-1}$ , corresponding to the mode of perfect graphite and a disordered breaking of symmetry within the crystal, respectively. The intensity of the  $1350 \text{ cm}^{-1}$  band in microcrystalline carbon is inversely proportional to grain size.

Amorphous carbon films have a Raman spectrum which is very broad and asymmetric, centered at roughly  $1540 \text{ cm}^{-1}$ . This peak actually has the same origin as the graphite peak, but is shifted by bond-angle disorder between atoms in  $sp^2$  sites. There is another broad peak present in amorphous diamond-like carbon with its center somewhere between  $1300$  and  $1350 \text{ cm}^{-1}$ . This peak, which corresponds to a shift in the microcrystalline carbon peak at  $1350 \text{ cm}^{-1}$ , is attributed to carbon atoms in  $sp^3$  sites.

#### Results of Sample Production

The surfaces of those samples included in this study displayed concentric ellipses of different shades of grey radiating outward from the sample center. These rings were caused by differences in the temperature and carbon concentration, which both decreased as the distance from the sample center increased. Comparisons of the Raman peak positions and widths of the different areas of the samples with the Raman signatures of the allotropes of carbon revealed

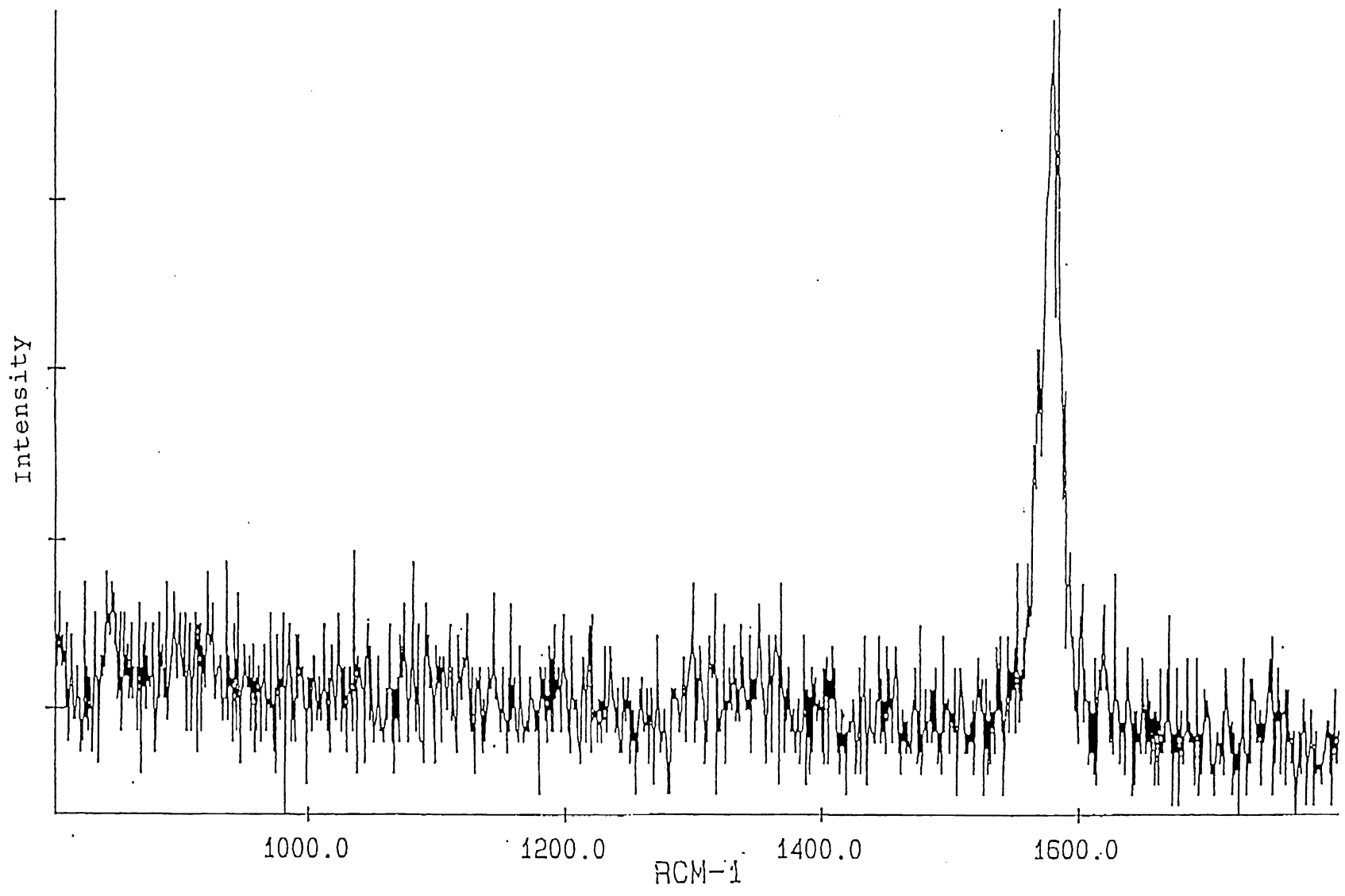


Figure 11. Typical Raman Spectrum of Graphite

the presence of different carbon forms in different rings. Those forms contained on the samples included not only diamond, graphite, microcrystalline carbon and a-C, but most importantly lonsdaleite, which has not previously been reported in CVD experiments. It is also important to add that several samples produced before the CVD apparatus was perfected contained a non-carbon substance which was later found to be tungsten carbide.

### Lonsdaleite

Small areas of high quality lonsdaleite were found on two samples, which had entirely different deposition parameters. Sample 2 (1.5% CH<sub>4</sub>/450 sccm) and sample 5 (4% CH<sub>4</sub>/175 sccm) both produced a Raman peak characteristic of lonsdaleite at 1320 cm<sup>-1</sup>, with FWHM values of 4.8 and 9.2 cm<sup>-1</sup>, respectively. A typical Raman spectrum of lonsdaleite produced in this study is shown in Figure 12.

The growth of lonsdaleite on sample 2 occurred in a ring located roughly 5mm from the center, while growth on sample 5 occurred in a far corner. Sample 2 contained a dense growth of grains of diameter 0.3 micrometers (μm) with cubic and triangular faces. Grains on sample 5 were less frequent, cubo-octahedral, and slightly larger, implying a lower nucleation rate, higher rate of growth, and fewer defects. Increased growth was attributed to a larger carbon concentration, while the reduction in defects was due to the

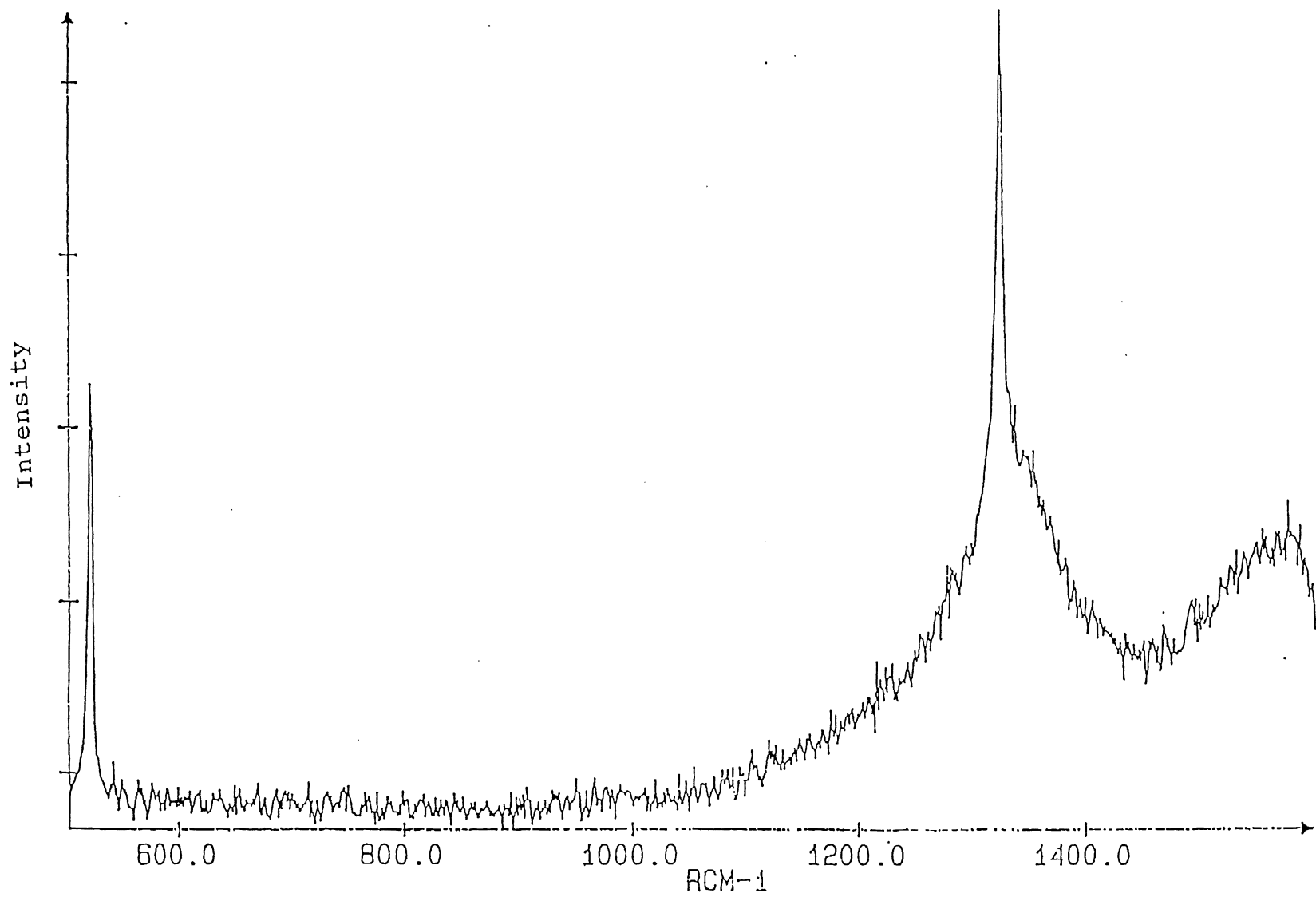


Figure 12. Typical Raman Spectrum of Lonsdaleite Produced in the Present Study

lower flow rate, which increased the surface reaction time of the carbon.

Although synthesized diamond doped with 36% of the  $^{13}\text{C}$  isotope shows a Raman peak identical to that of lonsdaleite, located at  $1319\text{ cm}^{-1}$ , naturally occurring carbon is composed of only 1.1% of the  $^{13}\text{C}$  isotope. Since the methane used in sample production was acquired from natural sources, it should also contain only 1.1%  $^{13}\text{C}$ , and it follows that any peaks near  $1319\text{ cm}^{-1}$  should be attributed to the presence of lonsdaleite, rather than a highly improbable  $^{13}\text{C}$  isotope concentration of 36%.

To eliminate the possibility of a calibration error in the Raman apparatus, which could cause the diamond peak at  $1332.5\text{ cm}^{-1}$  to shift to  $1319\text{ cm}^{-1}$  and falsely signify the presence of lonsdaleite, the position of the first order peak of the silicon substrate was examined. This peak, which should be located at  $520\text{ cm}^{-1}$ , would have to be incorrectly positioned at about  $507\text{ cm}^{-1}$  to shift the diamond peak to  $1319\text{ cm}^{-1}$ . For both samples, however, all Raman scans which showed a peak at  $1320\text{ cm}^{-1}$  also showed the silicon peak correctly positioned at  $520\text{ cm}^{-1}$ , supporting the presence of lonsdaleite.

### Diamond

Three samples showed Raman peaks which signified the presence of diamond. Sample 2 (1.5%  $\text{CH}_4/450\text{ sccm}$ ), sample 3 (2%  $\text{CH}_4/250\text{ sccm}$ ), and sample 4 (3%  $\text{CH}_4/100\text{ sccm}$ ) had Raman

peaks which ranged from 1329 to 1334  $\text{cm}^{-1}$  with peak widths from 4.4 to 13  $\text{cm}^{-1}$ . A typical Raman spectrum of diamond produced in this study is shown in Figure 13.

While most diamond-containing areas displayed a Raman peak at 1332.5  $\text{cm}^{-1}$ , agreeing with the position of natural diamond, some peaks were shifted by several wavenumbers. One scan for sample 3 showed a peak position of 1329  $\text{cm}^{-1}$ , while one for sample 4 showed a peak at 1334  $\text{cm}^{-1}$ . These shifts in peak position could be caused by stresses within the samples, with a positive shift associated with compression and a negative shift with tension. Given that the lattice constants of silicon and hexagonal silicon carbide are respectively larger and smaller than that of diamond, it is possible that the diamond on sample 3 is grown on a layer of silicon, while that on sample 4 is grown on silicon carbide. However, stress could also be caused by a lattice mismatch between the silicon substrate, oriented in the [100] direction, and the diamond grains, which grow in both the [100] and [110] directions, or by hydrogen inclusions within the diamond lattice, which could cause tensile stress as substitutional impurities or compressive stress as interstitials. Diamond growth occurred predominantly at the middle and outermost rings of the samples, where the temperature and carbon concentration were lowest. Since all methane concentrations used in this study were greater than values typically used in CVD diamond production, it makes sense that diamond growth would occur in the regions of more suitably

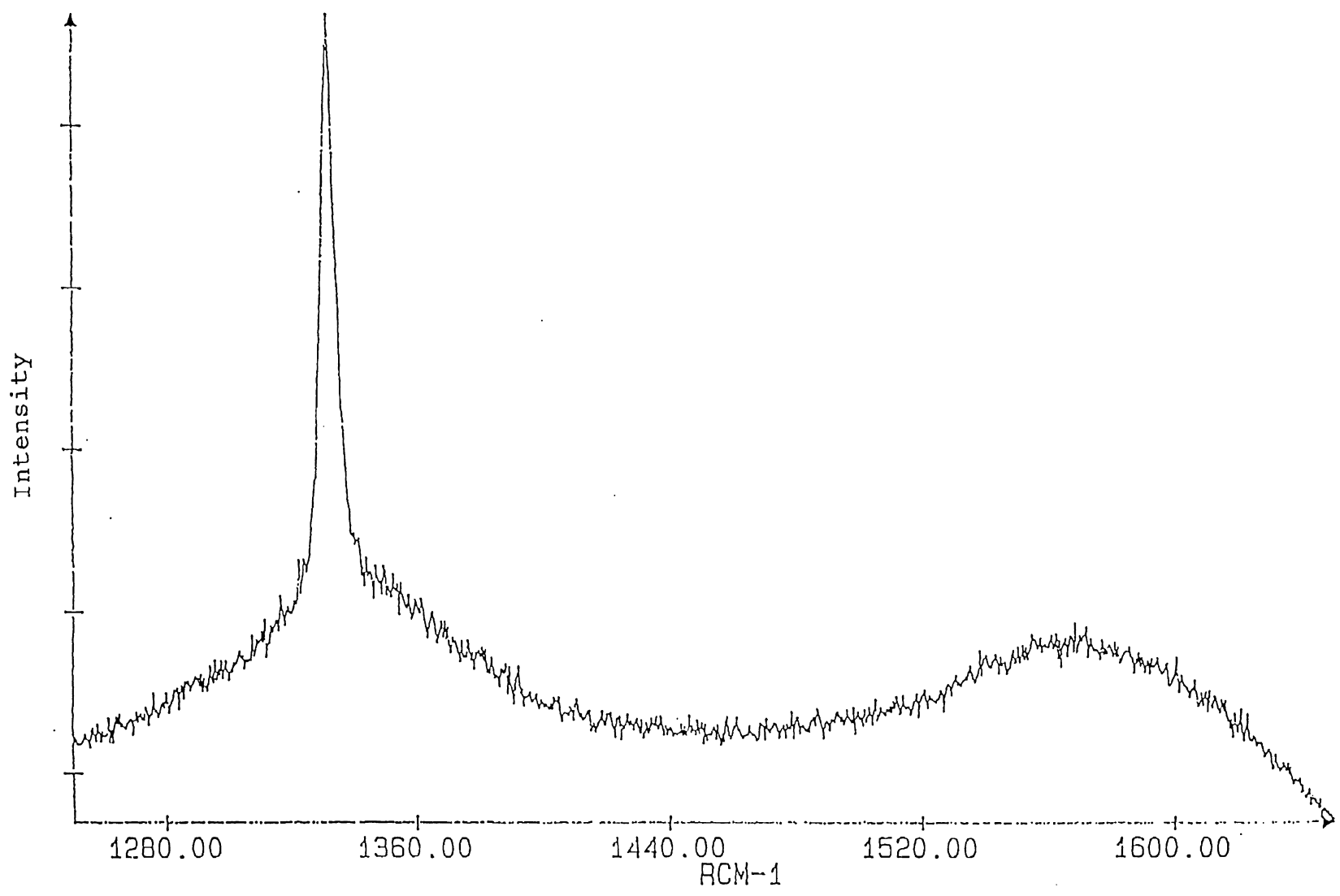


Figure 13. Typical Raman Spectrum of Diamond Produced in the Present Study

lower methane concentrations. While those grains closer to the center were cubic or triangular, those further from the center were cubo-octahedral or ball-like. The different morphologies are most likely due to differences in temperature, with grains closer to the center forming at higher temperatures and thus higher energies, so that the surface energy to volume ratio does not necessarily have to be at a minimum. With an average grain size of approximately  $0.3\mu\text{m}$  and an average deposition time of 3.5 hours, the rate of growth was roughly  $0.1\mu\text{m/hr}$ .

#### Other Allotropes of Carbon

Graphite, microcrystalline carbon, and amorphous carbon were all produced in this study. These allotropes are usually undesirable in CVD experiments, although their presence can be very useful in determining growth conditions suitable for both diamond and lonsdaleite.

Graphite was only present on two samples: sample 2 (1.5%  $\text{CH}_4/450$  sccm), and sample 6 (5%  $\text{CH}_4/200$  sccm). Both samples produced a peak characteristic of graphite at  $1576\text{ cm}^{-1}$ , as shown in Figure 14. With a FWHM value of  $20\text{ cm}^{-1}$ , the quality of the synthesized graphite is comparable to that of natural graphite. In both samples, growth occurred at the center, where the carbon concentration and temperature were the greatest. The carbon concentration in this area was so great that atomic hydrogen could not remove graphite as fast as it was being produced. Deposits ap-



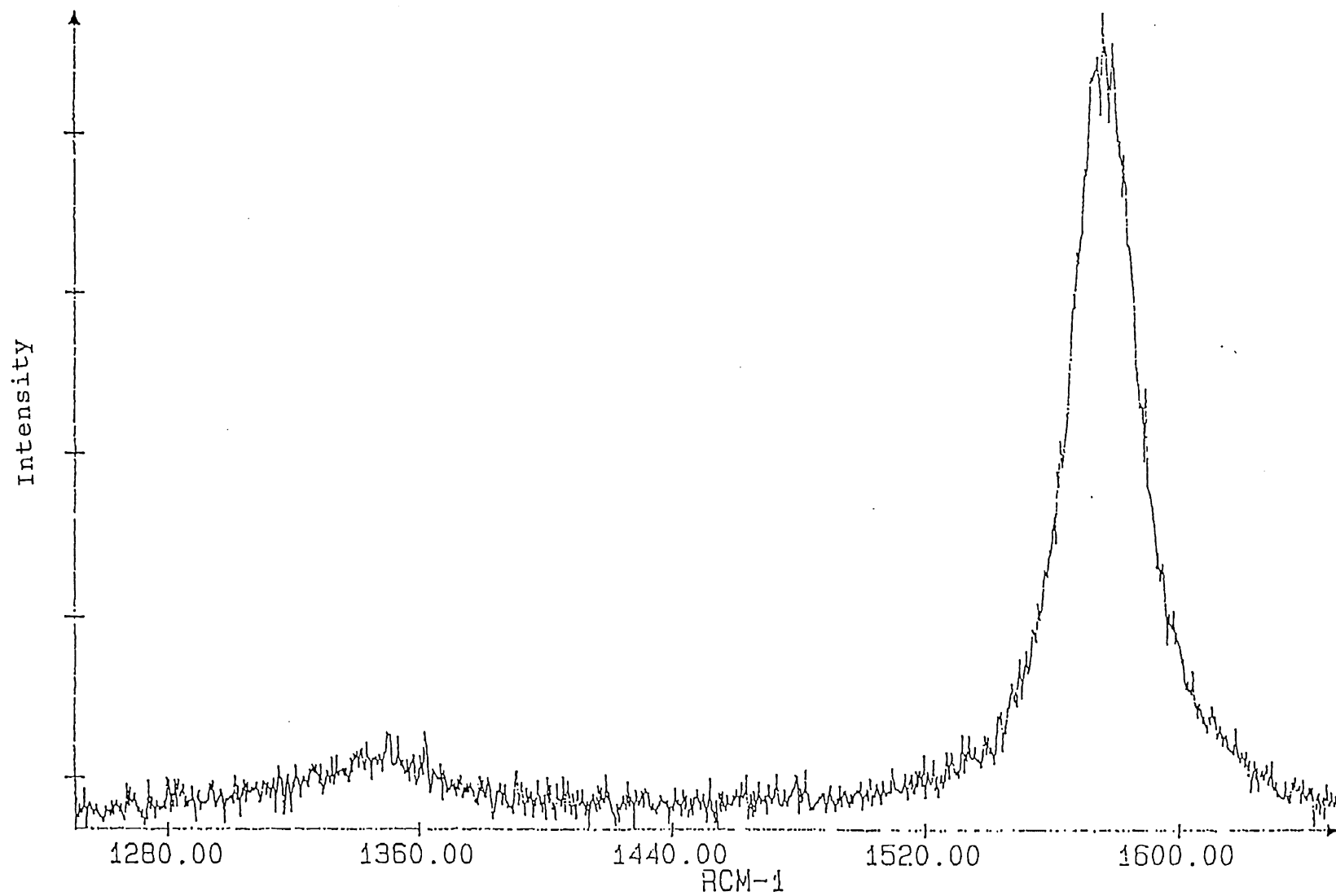


Figure 14. Typical Raman Spectrum of Graphite Produced in the Present Study

peared as dense, porous mounds of dark growth with tiny (25 nanometer (nm)), highly-reflective grains of graphite scattered throughout.

Regions of microcrystalline carbon were found on Samples 3 (2% CH<sub>4</sub>/250 sccm) and 4 (3% CH<sub>4</sub>/100 sccm), occurring chiefly at or near the center of each sample. In all scans, the first Raman peak was situated at about 1350 cm<sup>-1</sup>, while the second had its center between 1580 and 1590 cm<sup>-1</sup>. Both peaks were very broad, due to bond-angle disorder. A typical Raman scan of microcrystalline carbon produced in this study is shown in figure 15.

Grains on the surfaces of these two samples were completely different, with a dense population of dark balls of diameter 0.5µm on sample 3, and very fine crystalline granules of diameter 25nm on sample 4. Microcrystalline carbon most probably grew at the centers of samples 3 and 4 instead of graphite because parameters were such that the carbon concentration was only moderately high, allowing atomic hydrogen to remove graphite at a rate close to that at which it was produced, also affecting the grain size of the crystallites.

A mixture of amorphous carbon and microcrystalline carbon was present on all samples except numbers 2 and 6. A significant portion of this mixture was found all across samples 1 (3% CH<sub>4</sub>/500 sccm) and 5 (4% CH<sub>4</sub>/175 sccm), while 3 (2% CH<sub>4</sub>/250 sccm) and 4 (3% CH<sub>4</sub>/100 sccm) contained only smaller regions, located in the outermost ring and middle

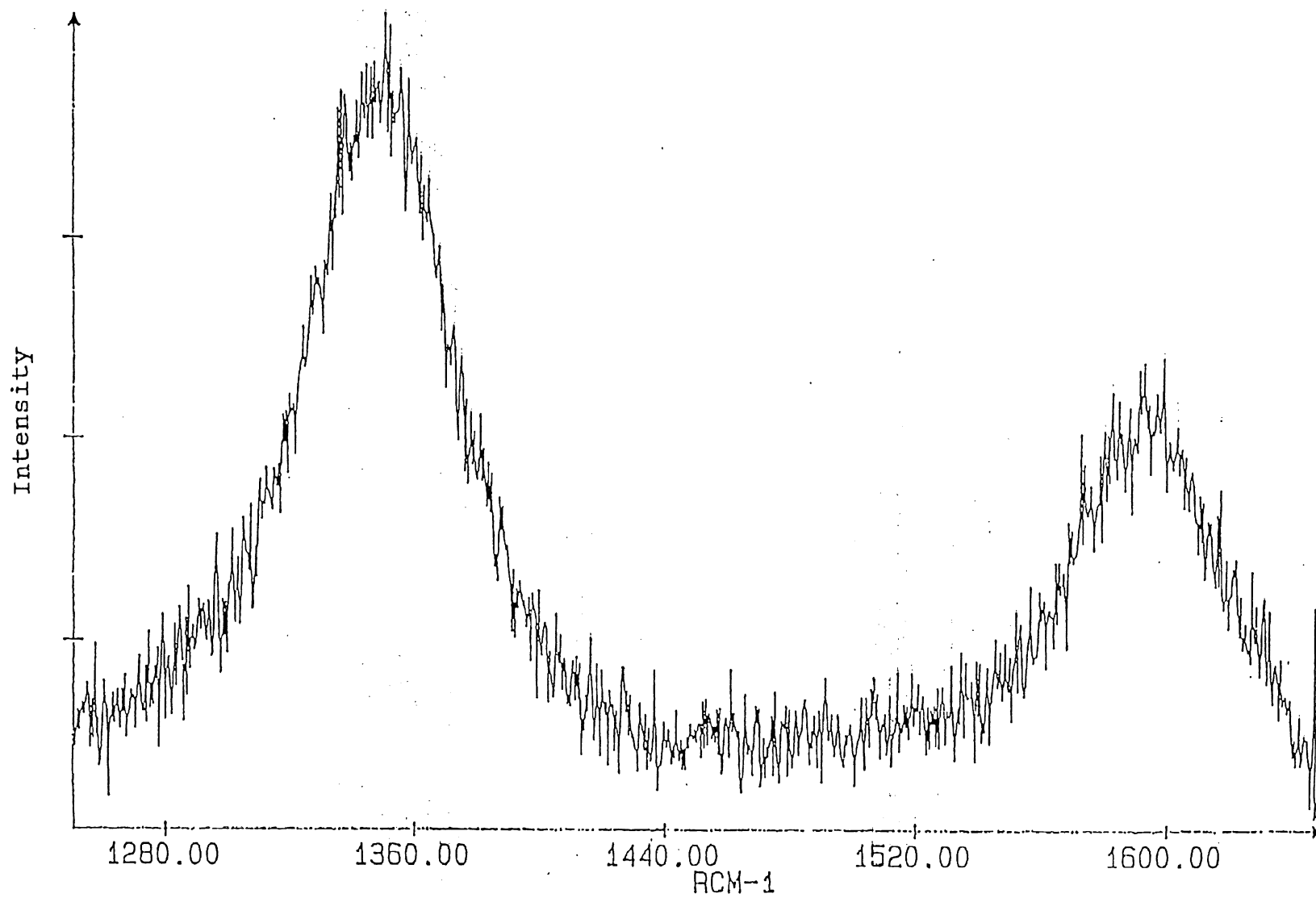


Figure 15. Typical Raman Spectrum of Microcrystalline Carbon Produced in the Present Study

ring, respectively. A Raman scan representative of this mixture is displayed in Figure 16, showing two broad peaks, the first at roughly  $1340\text{ cm}^{-1}$  and the second with its center between  $1558$  and  $1586\text{ cm}^{-1}$ . The first peak is typical of diamond-like a-C, while the second peak is closer to that of microcrystalline carbon, shifted from the a-C second peak position of  $1540\text{ cm}^{-1}$  to a position closer to the graphite peak, due to higher order among the  $sp^2$  bonds.

The a-C/microcrystalline carbon mixture seemed to follow a trend in morphology common to all samples. Those areas located closer to the sample center contained dark, roughly-textured balls of assorted diameters, which shifted to cubo-octahedral grains of  $0.3\mu\text{m}$  diameter further out, and then, at the outermost rings, to cubic and triangular facets. This mixture seemed to grow best when conditions were near those suitable for diamond growth, although the mixture grew for a wider range of carbon concentrations and temperatures than diamond. This seems reasonable, since the structures of both a-C and microcrystalline are much more disordered than diamond, and should require less energy to create.

### Tungsten Carbide

Several samples produced displayed a moderately sharp Raman peak at about  $842\text{ cm}^{-1}$  and smaller peaks at roughly  $920$  and  $1295\text{ cm}^{-1}$ , unlike any spectra of the allotropes of carbon. This recurring Raman spectrum, represented in Figure 17, seemed to occur over a wide range of deposition

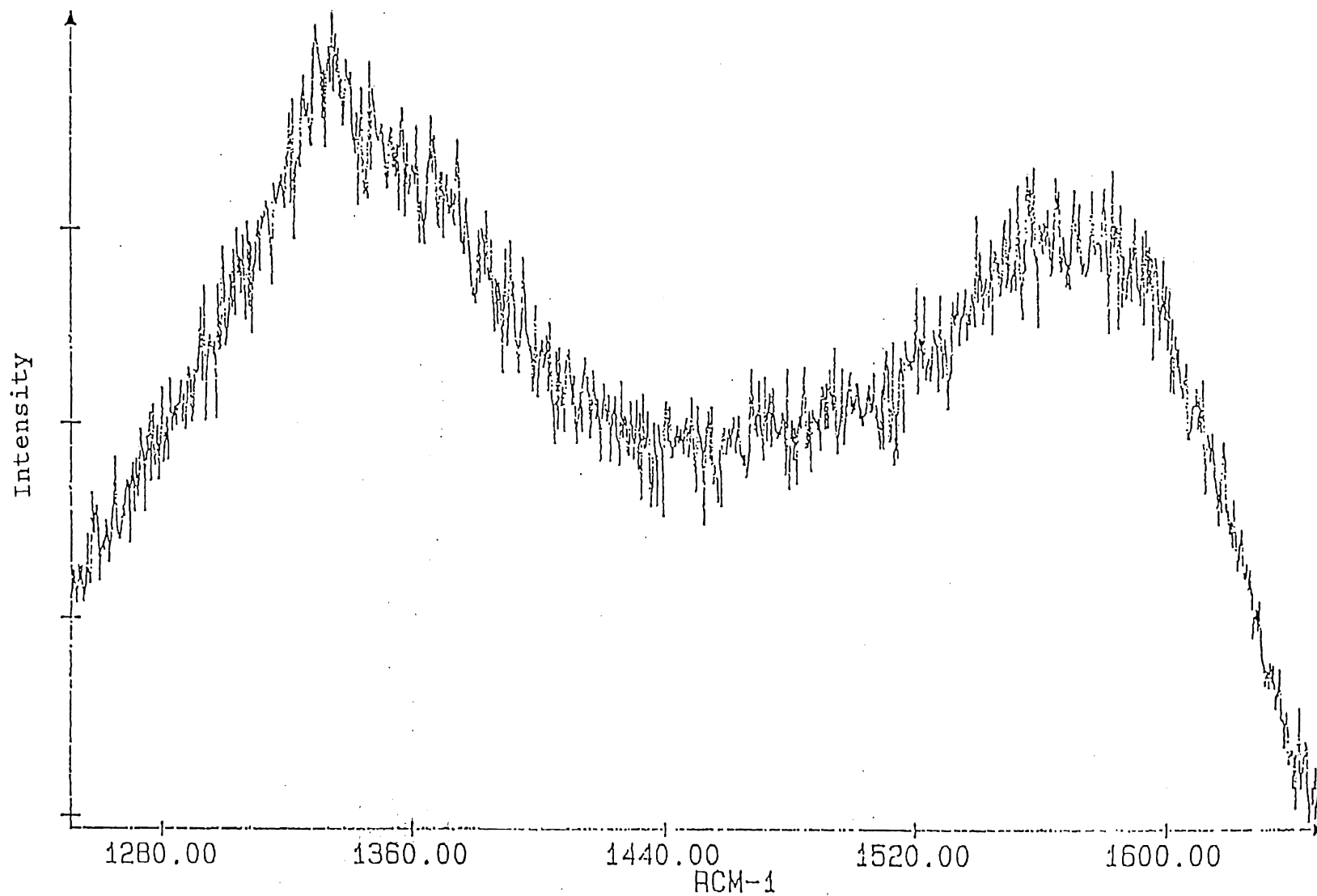


Figure 16. Typical Raman Spectrum of the Amorphous Carbon and Microcrystalline Carbon Mixture Produced in the Present Study

parameters but always coincided with a mass loss of the filament. Since the filament was composed of tungsten, Raman scans of pure samples of tungsten (W), tungsten silicide ( $WSi_2$ ), and tungsten carbide (WC) were made. The Raman spectrum of tungsten carbide, shown in Figure 18, agrees with that of the unknown substance.

There are two causes most probably responsible for the formation of tungsten carbide: either an excessive filament temperature or an inadequate distance between the filament and the substrate. A filament temperature greater than  $2000^{\circ}C$  would cause a large amount of tungsten to evaporate from the filament and react in the gas phase with carbon provided by the dehydrogenation of methane. This reaction would produce vapor phase tungsten carbide which would then be deposited on the silicon surface.

An inadequate distance between the filament and the substrate could also be the cause of tungsten carbide formation. At normal filament temperatures, there will always be some tungsten particles in the gas phase residing at the filament surface. If the substrate is too close, these molecules may attach to the surface and form a layer of tungsten silicide. Once the silicon is exhausted, surface reactions will occur between carbon and tungsten in the gas phase and tungsten already deposited on the surface.

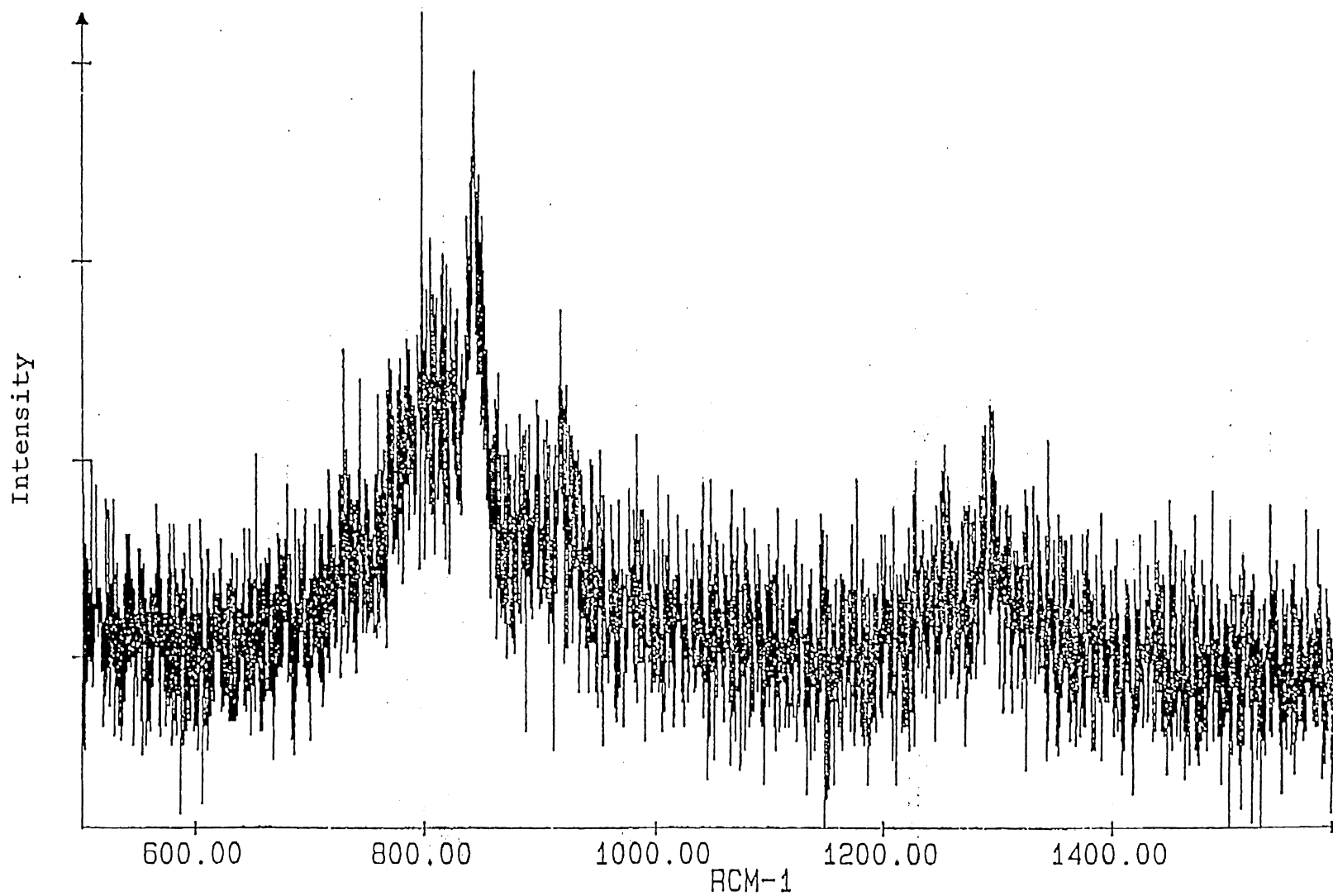


Figure 17. Recurring Raman Spectrum of Samples Produced Before the CVD Apparatus was Perfected

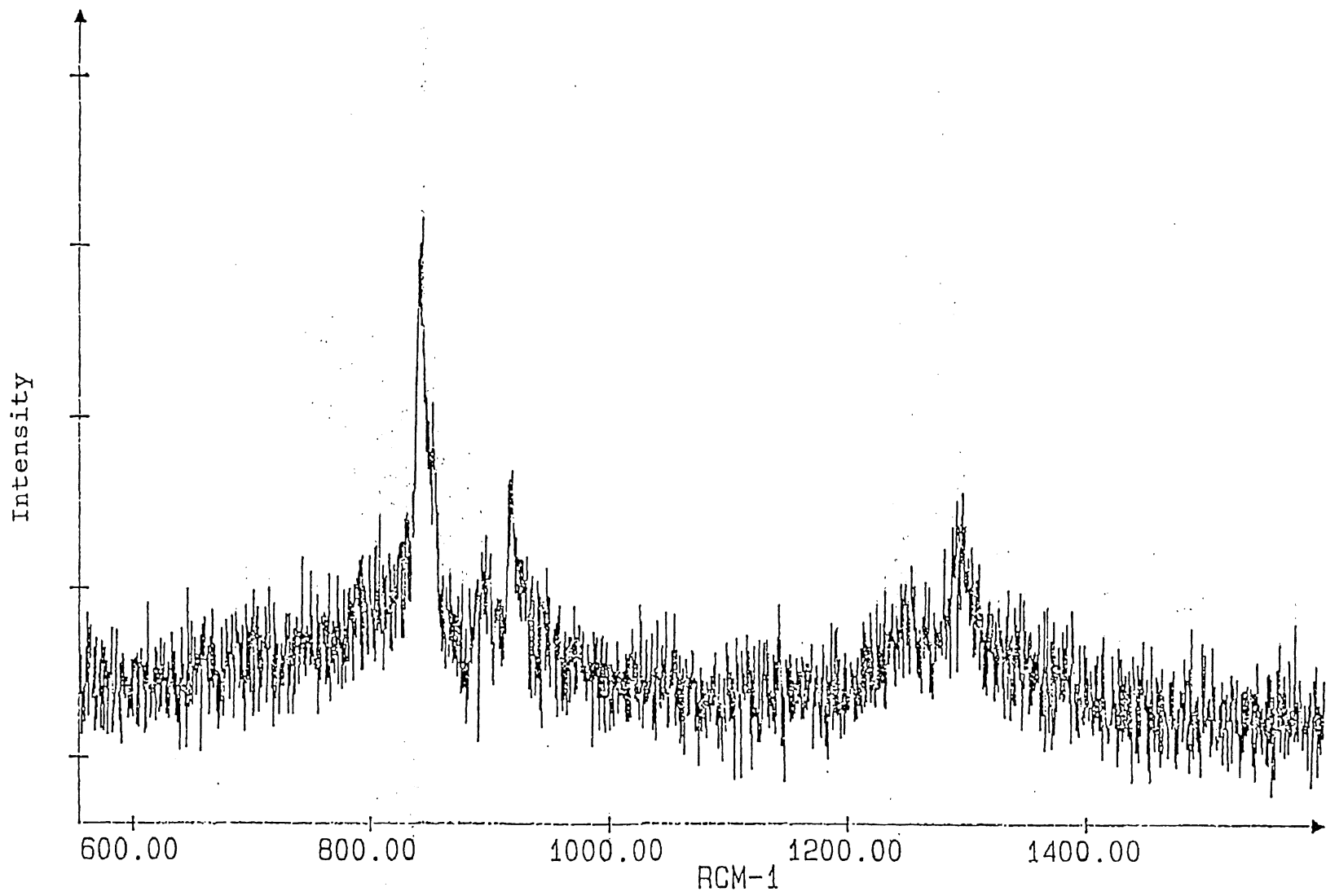


Figure 18. Typical Raman Spectrum of Tungsten Carbide



## CHAPTER 6

### DISCUSSION

In examining the growth trends of the different allotropes of carbon, a relationship is apparent between the preferential growth of diamond, graphite, microcrystalline carbon, and amorphous carbon and the qualitative concentration of carbon at the sample surface, which is a function of both the methane concentration and the total gas flow rate. As the carbon concentration decreases, preferred growth shifts from graphite to microcrystalline carbon and then to diamond and amorphous carbon.

The preferred growth of lonsdaleite is not included in the above relation because its trends in growth are not so obvious. Lonsdaleite was found to grow in small quantities near grains of diamond in sample 2 (1.5% CH<sub>4</sub>/450 sccm), but also near grains of the a-C mixture in sample 5 (4% CH<sub>4</sub>/175 sccm), implying that lonsdaleite grows over a different range of carbon concentrations than diamond, overlapping into the range favorable for the growth of the a-C mixture.

This overlapping could be related to the large number of defects included in the a-C mixture, with the presence of these defects being confirmed by the broadness of the Raman peaks. As mentioned previously, lonsdaleite and diamond may both grow from the hydrocarbon cage compound nuclei, al-

though the "boat" configuration of lonsdaleite is known to be less stable than the "chair" configuration of diamond. Carbon concentrations known to increase the defect density could easily increase the formation of high-energy "boat" defects as well. If these carbon concentrations were maintained, a high production of defects would persist, with "boats" being stacked upon "boats".

A proposed growth mechanism for lonsdaleite is shown in Figures 19. This model assumes reactions at the surface similar to those proposed by Frenklesh and Spear (28) for diamond, where hydrogen ions bound to the lonsdaleite surface would be removed by atomic hydrogen, allowing a reaction between a surface carbon radical and a hydrocarbon species in the gas phase to occur. At moderate carbon concentrations, the higher energy "boat" formations would occur frequently, not forming at all surface sites, but certainly a large portion of them. These "boat" formations would then lead to the growth of new lonsdaleite units.

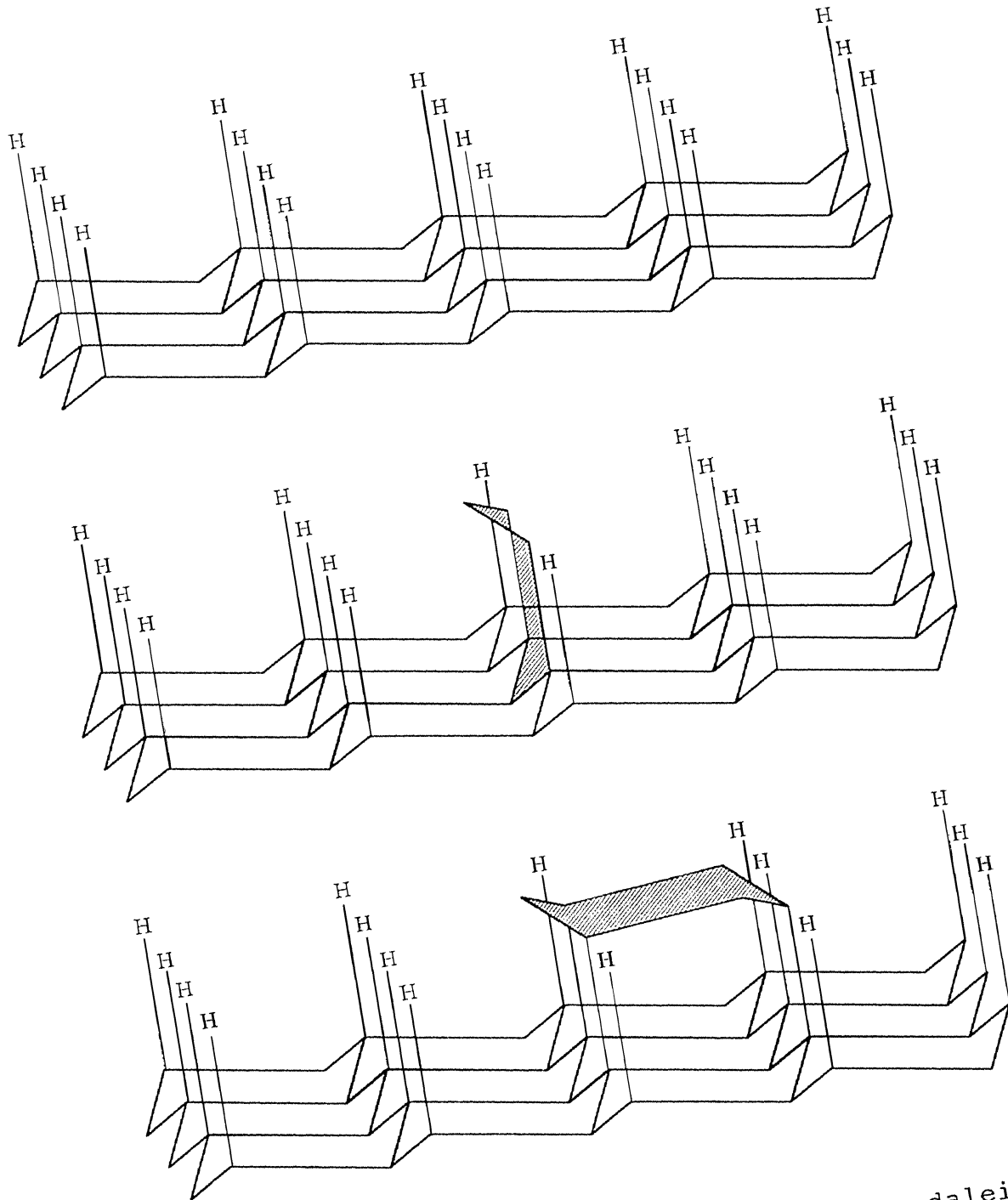


Figure 19. Proposed Growth Mechanism for Lonsdaleite: hydrogen ions stabilizing bonds at the lonsdaleite surface (top) are removed by atomic hydrogen, allowing reactions between surface carbon radicals and vapor-phase hydrocarbons (middle), which eventually result in the creation of new lonsdaleite units (bottom)

## CHAPTER 7

### SUMMARY AND SUGGESTIONS FOR FUTURE RESEARCH

In conclusion, the technique of filament-assisted chemical vapor deposition was used to produce not only diamond, graphite, microcrystalline carbon, and amorphous carbon, but also lonsdaleite, which has not previously been reported using CVD methods. Raman spectroscopy was used to determine which forms of carbon were present in samples, and the quality of crystalline structure. A relationship was observed between preferential growth and the qualitative carbon concentration at the surface, whereby preferred growth shifted from graphite to microcrystalline carbon and then to diamond and amorphous carbon as the carbon concentration decreased.

An explanation was offered as to the rare formation of lonsdaleite, suggesting that growth was due to a carbon concentration similar to that ideal for diamond, but overlapping into the region favorable for amorphous carbon. This overlap suggests that a larger defect density encourages the growth of lonsdaleite. A growth mechanism for lonsdaleite was also proposed.

The discovery of conditions favorable for the production of lonsdaleite by the CVD process is an important development in materials research. Lonsdaleite is known to be birefringent and has a more closely packed structure than dia-

mond, which implies extreme hardness. These properties alone make lonsdaleite a candidate for many optical applications. However, little else is known about the properties of this rare allotrope of carbon.

Future research will focus on several things, including attempts to produce larger regions of lonsdaleite by maintaining the ideal carbon concentration over a larger surface area, and to confirm the presence of lonsdaleite by x-ray diffraction techniques. Once these studies are performed, parameters other than the methane concentration and total flow rate should be varied, including the source gases and substrate material. Nitrogen or boron, which increase the hardness and semiconducting abilities of diamond, could be included in growth and substituted in the lonsdaleite lattice, possibly producing similar improvements. An additional research idea involves the study of strain at the diamond/substrate and lonsdaleite/substrate interfaces.

## REFERENCES

1. Eisenberg, Robert, and Resnick, Robert. Quantum Physics. United States: John Wiley and Sons, 1985.
2. Pierson, Hugh O. Handbook of Chemical Vapor Deposition. Park Ridge, New Jersey: Noyes Publications, 1992.
3. Phelps, A. W., J. Mater. Sci. Lett. 9, 1096 (1990).
4. Maruyama, K., Makino, M., Kikukawa, N., and Siraishi, M., J. Mater. Sci. Lett. 11, 116 (1992).
5. Weast, R. C., ed. CRC Handbook of Chemistry and Physics. 67th ed. Boca Raton, Florida: CRC Press, 1986.
6. Anderson, Herbert L., ed. A Physicist's Desk Reference. New York: American Institute of Physics, 1989.
7. Davis, Robert F. Diamond Films and Coatings. Park Ridge, New Jersey: Noyes Publications, 1993.
8. Bonnot, A. M., Phys. Rev. B 41, 6040 (1990).
9. Erskine, D. J., and Nellis, W. J., Nature 349, 317 (1991).
10. Hanneman, R. H., Strong, H. M., and Bundy, F. P., Science 155, 995 (1967).
11. Davanloo, F., Juengerman, E. M., Jander, D. R., Lee, T. J., and Collins, C. B., J. Appl. Phys. 67, 2081 (1990).
12. Yarbrough, W. A., and Messier, R., Science 247, 688 (1990).
13. Joffreau, P. O., Haubner, R., and Lux, B., in: Diamond and Diamond-Like Materials Synthesis, April 1988, Ed. Johnson, G. H., Badzian, A. R., and Geis, M. W., Materials Research Society, 1988 (pp. 15 to 18).
14. Popovici, G., and Prelas, M. A., Phys. Stat. Sol. (a) 132, 233 (1992).

15. Williams, B. E., Glass, J. T., Davis, R. F., and Kobashi, K., *J. Cryst. Growth* 99, 1168 (1990).
16. Williams, B. E., and Glass, J. T., *J. Mater. Res.* 4, 373 (1989).
17. Badzian, A. R., *Mater. Res. Bull.* 23, 385 (1988).
18. Matsumoto, S., and Matsui, Y., *J. Mater. Sci.* 18, 1785 (1983).
19. Ling, P. X., *Mater. Sci. and Eng.* B14, L15 (1992).
20. F. G. Celii, D. White, Jr., and A. J. Purdes, *J. Appl. Phys.* 70, 5636 (1991).
21. Kim, J.W., Baik, Y. J., and Eun, K. Y., in: Applications of Diamond Films and Related Materials, August 1991, Ed. Y. Tzeng, M. Yoshikawa, M. Murakawa, and A. Feldman, Elsevier Sci. Publ., 1991 (pp. 399 to 403).
22. Chang, J. J., Mantei, D., Vuppuladhadiam, R., and Jackson, H. E., *Appl. Phys. Lett.* 59, 1170 (1991).
23. Decker, R. F., Fournier, E. W., Asmussen, J., Bigelow, K., and Hoggins, J., *Microwave Processing for Diamond Films*, distributed by Wavemat, Inc.
24. Kim, J. S., Kim, M. H., Park, S. S., and Lee, J. Y., *J. Appl. Phys.* 67, 3354 (1990)
25. Kumagai, K., Miyata, K., Nishimura, K., and Kobashi, K., *J. Mater. Res.* 8, 314 (1993).
26. Zhu, W., Randall, C., Badzian, A. R., and Messier, R., *J. Vac. Sci. Technol. A* 7, 2315 (1989).
27. Meilunas, R., Wong, M. S., Sheng, K. C., and Chang, R. P. H., *Appl. Phys. Lett.* 54, 2204 (1989).
28. Frenklash, M., and Spear, K., *J Mater. Res.* 3, 133 (1988).
29. Muranka, Y., Yamashita, H., and Miyadera, H., *J. Appl. Phys.* 69, 8145 (1991).
30. Kawato, T., and Kondo, K., *Jap. J. Appl. Phys.* 26, 1429 (1987).
31. N. Uchida, T. Kurita, K. Uematsu, and K. Saito, *J. Mater. Sci. Lett.* 9, 249 (1990).

32. N. Uchida, T. Kurita, K. Uematsu, and K. Saito, J. Mater. Sci. Lett. 9, 251 (1990).
33. Frondel, C., and Marvin, U. B., Nature 214, 587 (1967).
34. Gilson, T. R., and Hendra, P. J. Laser Raman Spectroscopy. Bath, Great Britain: Dawson and Goodall Ltd., The Mendip Press, 1970.
35. Anderson, A., ed. The Raman Effect, vol 1. New York: Marcel Dekker, Inc., 1971.
36. Schroder, R. E., and Nemanich, R. J., Phys. Rev. B 41, 3738 (1990).
37. Buckley, R. G., Moustakas, T. D., Ling, Y. and Varon, J., J. Appl. Phys. 66, 3595 (1989).
38. Knight, D. S., Drawl, W. R., Badzian, A. B., Badzian, T., and White, W. B., in: Diamond and Diamond-Like Materials Synthesis, April 1988, Ed. Johnson, G. H., Badzian, A. R., and Geis, M. W., Materials Research Society, 1988 (p.73).
39. Wolden, C, Mitra, S., and Gleason, K. K., J. Appl. Phys. 72, 3750 (1992).



VITA

Karen Elaine Suhm

Candidate for the Degree of

Master of Science

Thesis: SYNTHESIS OF LONSDALEITE BY FILAMENT-  
ASSISTED CHEMICAL VAPOR DEPOSITION

Major Field: Physics

Biographical:

Personal Data: Born in Kingsville, Texas, December 10,  
1970, the daughter of Dr. Raymond Walter Suhm and  
June Elaine (Gillespie) Suhm.

Education: Graduated from Moore High School, Moore,  
Oklahoma, in May, 1989; received Bachelor of  
Science degree with Honors in Physics and  
Mathematics from Oklahoma State University,  
Stillwater, Oklahoma, in December, 1991; completed  
the requirements for the Master of Science degree  
in Physics at Oklahoma State University in  
December, 1993.

Experience: Employed by Oklahoma State University,  
Department of Physics as an undergraduate teaching  
assistant, 1991, and as a graduate research  
assistant, 1992 to present.